Fabrication of metal nanoparticles in metal–organic frameworks†

Hoi Ri Moon,[a] Dae-Woon Lim[b] and Myunghyun Paik Suh*[b]

In this review, we highlight various preparative strategies and characterization methods for metal nanoparticles fabricated in porous metal–organic frameworks (MOFs) or porous coordination polymers (PCPs), and their applications in hydrogen storage and heterogeneous catalysis.

1. Introduction

Metal–organic frameworks (MOFs) are the materials that are constructed by connectivity of metal ions and multidentate organic building blocks. MOFs are also called porous coordination polymers (PCPs) or coordination polymer networks (CPNs).[1] Most of these solid materials possess well-defined pores and large internal surface areas. Although permanent porosity cannot be always generated in MOFs, it is a useful property

for the applications. By selecting appropriate inorganic and organic building blocks, the rational design of framework structures having desired pore size and shape is feasible.[2] Easy functionalization and modification of the inner pore surface are also important features of MOFs.[3] Well-designed MOFs can be applied in gas storage and separation,[4] heterogeneous catalysis,[5] molecular recognition and sensing,[6] and optics.[7]

Recently, there have been extensive efforts to fabricate metal-nanoparticles (M-NPs) in MOFs to elicit the properties that are hardly achieved by the individual material.

The physical and chemical properties of M-NPs are different from those of bulk metals, such as thermal and electrical conductivities, which are manifested by delocalization of free electrons.[8] Since the high surface-area-to-volume ratio of M-NPs provides a large number of active sites, the size and shape control of M-NPs is the key to achieve enhanced reactivity.[9] However, as a consequence of the high surface energy and large surface area

[a] *Interdisciplinary School of Green Energy and KIER-UNIST Advanced Center for Energy, Ulsan National Institute of Science and Technology, Ulsan 689-798, Republic of Korea. E-mail: hoirimoon@unist.ac.kr; Fax: +82-52-217-2019; Tel: +82-52-217-2928*

[b] *Department of Chemistry, Seoul National University, Seoul 151-747, Republic of Korea. E-mail: mpsuh@snu.ac.kr; Fax: +82-2-886-8516; Tel: +82-2-880-7760*

† Part of the centenary issue to celebrate the Nobel Prize in Chemistry awarded to Alfred Werner.

Hoi Ri Moon received her BS degree from the Department of Chemistry, Ewha Womans University (2001), and MS (2003) and PhD (2007) from Seoul National University under the direction of Professor Myunghyun Paik Suh. After postdoctoral work with Dr Jeffrey J. Urban at Lawrence Berkeley National Lab, she became an assistant professor at the Interdisciplinary School of Green Energy, Ulsan National Institute of Science and Technology (UNIST) in 2010. Her research interests are nanostructured inorganic materials for energy applications.

Hoi Ri Moon

Dae-Woon Lim received his BS (2009) degree in chemistry from DanKook University in Korea. He is currently a PhD student at Seoul National University, working on porous materials and nanocomposites for hydrogen storage under the guidance of Prof. Myunghyun Paik Suh.

Dae-Woon Lim

This journal is © The Royal Society of Chemistry 2013

Chem. Soc. Rev., 2013, **42**, 1807–1824 | **1807**

of M-NPs, their thermodynamic stability is severely decreased, which obstructs the control of size and shape with high uniformity. Various synthetic methods have been exploited to obtain monodispersed and small-sized M-NPs. To control the nucleation and growth of M-NPs, an organic surfactant or a polymer has been introduced as a surface capping agent,[10] or M-NPs have been enclosed within an inorganic material such as silica to form a core–shell structure.[11]

Another approach is to produce M-NPs inside porous inorganic materials with defined pore size such as zeolites, mesoporous aluminosilicates, and other porous inorganic or organic materials.[12] In particular, MOFs have been utilized as supports for M-NPs since they control the limited growth of M-NPs in the confined cavities, and produce monodispersed M-NPs.[13]

Utilization of MOFs as supports for M-NPs has several advantages over other porous materials; their three dimensional pore structures, the presence of organic linkers that stabilize M-NPs, robust structural property in some cases, and moderate thermal stability. Various MOFs with different pore sizes and shapes can be prepared from a wide range of metal ions and organic linkers, and thus an appropriate MOF can be easily selected as a host matrix. In choosing a MOF for loading M-NPs, the structural stability of the MOF upon the precursor loading or reduction procedure should be considered. Furthermore, to maintain a high surface area of the MOF, caution must be taken in the reduction process not to block the pores by the NPs or by unwanted by-products formed. Although the encapsulation of M-NPs in MOF pores is expected to limit the particle growth, the precursor compound and the product can actually diffuse out through the pores of the host to form M-NPs on the surface of the MOF crystal, instead of being inside the pores. Therefore, the location of the M-NPs, on the surface of the crystal or inside of the pores, should be verified by experimental evidence. If MOFs have straight channels, they do not provide an adequate confinement effect, and thus there is a possibility that agglomeration may occur and M-NPs may escape through the pores. Therefore, it is necessary to develop novel porous MOFs that can be employed as supports for M-NPs for the improvement of efficiency.

Myunghyun Paik Suh

Myunghyun Paik Suh is a professor in the Department of Chemistry at Seoul National University. She received her BS from Seoul National University (1971) and PhD from the University of Chicago (1976), and started her career as an assistant professor at the Seoul National University in 1977. Her current research interest is the development of energy and environment related materials based on coordination chemistry and nanoscience. She is a member of the Korean Academy of Science and Technology, and has received the Korean Science Award offered by the President of Korea.

M-NPs@MOF can be applied to hydrogen storage[14,15] and heterogeneous catalysis, depending on the type of metal.[16–20] For example, Pd-NPs@MOF has shown enhanced hydrogen storage both at 77 K and at room temperature.[14] In particular, Mg-NPs@MOF adsorbs hydrogen by physisorption at low temperatures and by chemisorption at high temperatures, exhibiting a synergistic effect on both adsorptions.[21] The material increases isosteric heat of hydrogen physisorption and decreases significantly the hydrogen chemisorption/desorption temperatures compared to Mg powder. Furthermore, some M-NPs@MOFs have exhibited excellent catalytic activities in organic reactions due to the confinement effect of the substrates in a MOF as well as the limitation of the particles that remain constrained and do not grow further after catalytic reactions.

A couple of years ago, Fischer et al. published a wonderful review entitled "Metals@MOFs – Loading MOFs with Metal Nanoparticles for Hybrid Functions".[13] The paper described the preparation and characterization methods of M-NPs@MOF materials as well as some useful applications. In the present tutorial review, we embrace the recent progress in the development of M-NPs@MOF systems, including previously reviewed systems, and cover the advanced characterization techniques and more extensive applications. In particular, we discuss some important issues that have arisen in this field of research such as size control of M-NPs in MOFs, localized destruction of frameworks in M-NPs@MOFs, and location of M-NPs in MOFs.

2. Various methods of preparation

General synthetic methods to embed M-NPs in a porous solid matrix entail the impregnation of a metal precursor in a porous solid, followed by reduction of the metal precursor to metal(0) atoms, which aggregate into M-NPs within the solid matrix. The precursor molecules that are most frequently used for the production of M-NPs are chloride or nitrate salts of the corresponding transition metal ions. In addition, organometallic complexes are often used as precursors in the solid grinding or infiltration method.[22] In general, metal precursors included in MOFs are reduced with hydrogen gas, hydrazine, or NaBH$_4$ to generate M-NPs, and the reduction process is often performed at high temperature, followed by a washing step. In some cases, supercritical CO$_2$-methanolic solution has been used to load the precursor compound within a MOF, followed by a heating process.[23] The reaction conditions for fabricating M-NPs in MOFs should be determined depending on the properties of the included precursors as well as the stability of the host matrices during the reduction process. Since the size of the NPs is significantly affected by the loading time of the metal precursor and the reduction conditions, these conditions should be carefully controlled.

2.1 Simple immersion of redox active MOFs in metal salt solutions

Contrary to the conventional methods, Suh's group developed new fabrication methods for M-NPs in PCPs, which produced M-NPs without using any capping or reducing agents and with

1808 | Chem. Soc. Rev., 2013, 42, 1807–1824

This journal is © The Royal Society of Chemistry 2013

no heating process at all.[14,24–27] They used redox active PCPs as supports for M-NPs and immersed them in the solutions of metal salts such as AgNO$_3$, NaAuCl$_4$, and Pd(NO$_3$)$_2$. They prepared redox active PCPs by using redox active building blocks. Redox active sites of the redox active building blocks may be at the organic ligands or at the metal centers such as Ni(II) sites in the Ni(II) macrocyclic complexes. As soon as metal ions are diffused into the redox active PCPs, they are reduced to metallic nanoparticles and the redox active building blocks in the PCPs are oxidized. The maximum amount of M-NPs formed can be easily predicted since the redox reactions between the redox active networks and metal ions are stoichiometric. In most of the cases, the redox active PCPs retain their network structures even after the formation of M-NPs that are commonly much larger than the pore size of the PCPs. The most important advantage of this method is that the amount of M-NPs loaded in the PCP can be controlled by the immersion time of the host solid in the metal ion solution, while the size of the M-NPs is unaffected by the immersion time, concentration of the metal ion solution, temperature, and the type of solvent.

Suh's group employed various Ni(II) square-planar macrocyclic complexes as redox active metal building blocks to construct redox-active PCPs.[24–27] The Ni(II) macrocyclic complexes were prepared by simple one-pot template Schiff base condensation reactions.[28] They synthesized PCPs by self-assembly of the Ni(II) macrocyclic complexes and multidentate organic ligands containing carboxylate donor groups. The Ni(II) ion of the macrocyclic complex has a square planar coordination geometry and coordinates to the carboxylate ligands through the axial positions to generate octahedral geometry. Therefore, the Ni(II) macrocyclic complex simply acts as *a linear linker* to connect the organic ligand in the construction of PCPs. By selecting organic building blocks of various topologies, PCPs whose topology can be easily predicted from the geometry of organic ligands are constructed. The octahedral Ni(II) macrocyclic complexes can be easily oxidized to Ni(III) species.[28] The oxidation potential of Ni(II) to Ni(III) in the monomacrocyclic complexes is in the range of +0.90–+0.93 V vs. SCE in acetonitrile solutions.[28] When the PCPs constructed from Ni(II) macrocyclic complexes in octahedral coordination mode react with appropriate noble metal ions, oxidized PCPs with Ni(III) macrocyclic species and metal(0) nanoparticles result. Various Ni(II) macrocyclic complexes employed in the construction of redox active PCPs are shown in Fig. 1.[24–27]

The self-assembly of (NiL$_1$)(ClO$_4$)$_2$ (NiL$_1^{2+}$ = [Ni(C$_{10}$H$_{26}$N$_6$)]$^{2+}$) and Na$_2$bpdc (bpdc^{2-} = 4,4'-biphenyldicarboxylate) in a H$_2$O–pyridine mixture resulted in [(NiL$_1$)$_3$(bpdc)$_3$]·2pyridine·6H$_2$O (1), in which linear coordination polymer chains pack as a double network of threefold braids to generate 1D channels with honeycomb-shaped
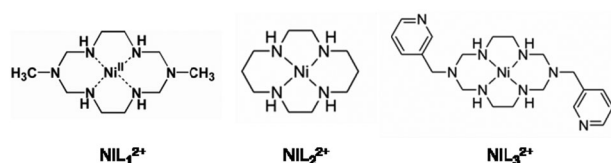

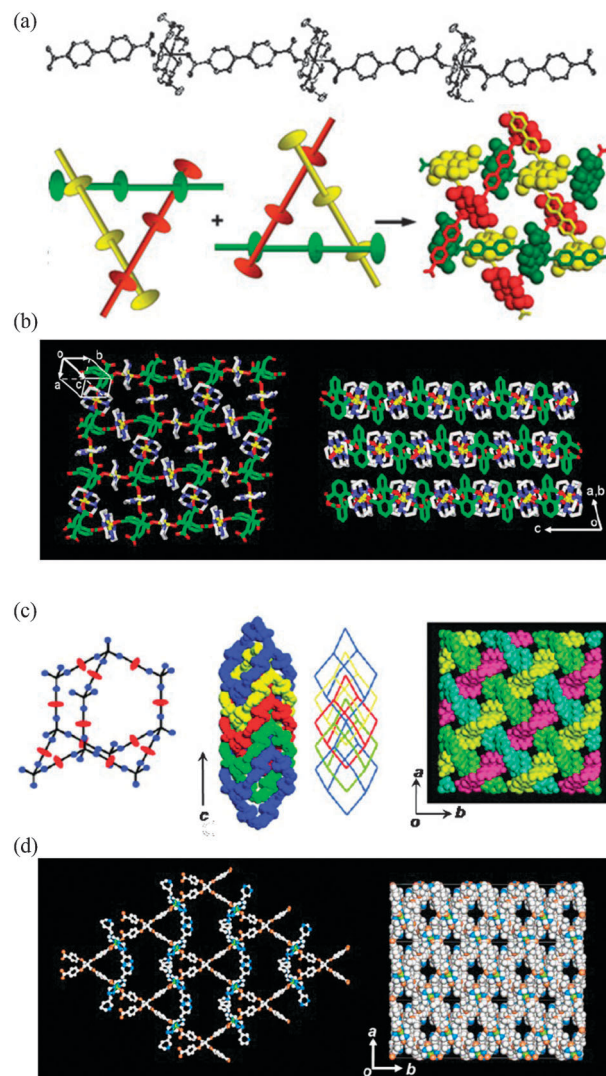**Fig. 1** Chemical structures of Ni(II) macrocyclic complexes as redox active species.

Fig. 2 X-ray structure of porous coordination polymer (a) [(NiL$_1$)$_3$(bpdc)$_3$]·2pyr·6H$_2$O (1), (b) [(NiL$_2$)$_2$(bptc)]·2H$_2$O (2), (c) [(NiL$_2$)$_2$(mtb)]·8H$_2$O·4dmf (3), and (d) [(NiL$_3$)$_2$(tcm)]·5dmf·8H$_2$O (4). Reprinted with permission from ref. 24–27.

windows (effective pore size, 7.3 Å) (Fig. 2a).[24] When desolvated host 1 was immersed in a methanolic solution of AgNO$_3$ (8.0 × 10^{-2} M) at room temperature for 10 min, Ag NPs (ca. 3 nm in diameter) were formed in solid 1. Inclusion of Ag(I) ions into 1 resulted in the oxidation of incorporated Ni(II) species to Ni(III) and simultaneous reduction of Ag(I) to Ag(0), followed by the nucleation and growth of Ag NPs. The redox reaction between Ag(I) and Ni(II) species was proved by electron paramagnetic resonance (EPR) spectroscopy indicating the presence of d^7 Ni(III) species ($g_\perp > g_\parallel$) together with X-ray photoelectron spectroscopy (XPS) showing the coexistence of Ni(III) and Ag(0). Elemental analysis data for the solid composite isolated after immersion of 1 in AgNO$_3$ solution for 10 min indicated that the reaction stoichiometry of Ni^{II} in the host matrix and AgNO$_3$ was 1 : 1, proving that the redox reaction is quantitative. Since the host framework became positively charged after the redox reaction, it included free NO$_3^-$ anions as shown by the unsplit 1382 cm^{-1}

peak in the IR spectra. The powder X-ray diffraction (PXRD) patterns indicated that the framework structure was retained even after the formation of Ag NPs, and the peaks corresponding to Ag NPs were extremely weak due to the very small sized NPs and too little Ag compared to the amount of the host solid. Introducing well-designed building blocks into PCPs, the single-step preparation method for M-NPs in the solid support was successfully developed without using reducing agents and stabilizing agents at room temperature. The average size of the M-NPs was independent of immersion time, concentration of the metal salts, type of solvents, and temperature. Most interestingly, despite the formation of the metal nanoparticles, PXRD patterns of the network were intact, suggesting that network structure was unaltered by the metal NPs that are much bigger than the aperture size of the network. This was because even if all M-NPs break down the network, less than 10% of the whole framework would be destroyed and thus most of the network would be retained.

By similar methods, Au and Pd NPs were also fabricated in the redox active PCPs. As shown in Fig. 2b, the two dimensional square grid coordination network $[(NiL_2)_2(bptc)]\cdot 2H_2O$ (2) was assembled from $(NiL_2)(ClO_4)_2$ (L_2 = 1,4,8,11-tetraazacyclotetradecane) and H_4bptc ($bptc^{4-}$ = 1,1′-biphenyl-2,2′,6,6′-tetracarboxylate). When 2 was immersed in EtOH solutions of $AgNO_3$ and $NaAuCl_4$ for 5 min, Ag NPs (3.7 ± 0.4 nm) and Au NPs (*ca.* 2 nm), respectively, were formed in the network.[25] In 2, two dimensional layers of about 1 nm thickness were stacked with an interlayer spacing of 9.3 Å, through which $AgNO_3$ or $NaAuCl_4$ diffused and then their metal ions were reduced to Ag(0) and Au(0) NPs, respectively. Within 5 min of immersion in 0.1–0.3 M metal ion solution, redox reaction between the metal ions and the network occurred quantitatively, and all Ni(II) macrocyclic species were oxidized to Ni(III) to form Ag(0) NPs (*ca.* 4 nm) and Au(0) NPs (*ca.* 2 nm). This was characterized by elemental analyses, which indicated the inclusion of counter anions NO_3^- and Cl^-, respectively.

To fabricate small-sized Pd NPs in the PCPs, two redox active PCPs, $[(NiL_2)_2(mtb)]\cdot 8H_2O\cdot 4dmf$ (mtb^{4-} = methanetetrabenzoate, dmf = *N*,*N*′-dimethylformamide) (3) (Fig. 2c) and $[(NiL_3)_2(tcm)]\cdot 5dmf\cdot 8H_2O$ ($L_3 = C_{20}H_{32}N_8$; tcm^{4-} = tetrakis[4-(carboxyphenyl)-oxamethyl]methane) (4) (Fig. 2d), were prepared by the self-assembly of corresponding Ni(II) macrocyclic complexes and organic building blocks.[26,27] The PCP 3 has a fourfold interpenetrated diamondoid network generating 1D channels with ink-bottle-type pores having a big cavity (13.4 × 13.4 Å) connected with narrow necks (2.05 × 2.05 Å).[26] Immersion of the desolvated solid of 3 in an acetonitrile solution of $Pd(NO_3)_2$ resulted in 2 nm-sized Pd NPs by autoredox reaction between Ni(II) macrocyclic species incorporated in the network and Pd(II) ions. Similarly, network 4 constructed by doubly catenated rhombic grids that generate 1D channels (effective window size, 4.5 × 2.1 Å) also produced Pd NPs of 3 nm size.[27]

Suh's group also prepared redox active PCPs by using redox active organic building blocks.[14] Since 4,4′,4″-nitrilotrisbenzoate (ntb^{3-}) can be readily oxidized to the amine radical, the PCP constructed from ntb^{3-} becomes redox active as shown in Fig. 3.
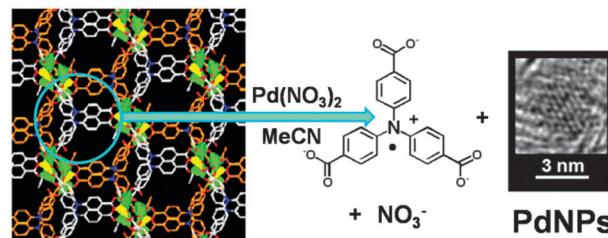
Fig. 3 Reaction of a MOF (5) incorporating redox-active organic species, 4,4′,4″-nitrilotrisbenzoate (ntb^{3-}), with Pd^{2+} ions. Reproduced with permission from ref. 14.

When a porous MOF, $[Zn_3(ntb)_2(EtOH)_2]\cdot 4EtOH$ (EtOH = ethyl alcohol) (5),[29] which was synthesized from the solvothermal reaction of H_3ntb and $Zn(NO_3)_2$, was immersed in the acetonitrile solution of $Pd(NO_3)_2$ (1.0×10^{-3} M) for 30 min, the Pd(0) NPs of size 3.0 ± 0.4 nm were formed in the channels (aperture size, 7.7 Å) of the MOF.[14] The EPR spectrum indicated that the MOF was oxidized to the positively charged network with the nitrogen radical. The amount of Pd NPs loaded in the MOF could be controlled by the immersion time in the metal ion solution, which in turn affected the H_2 uptake. The MOF embedded with 3 wt% Pd NPs adsorbed the highest amount of H_2 at 77 K and 1 atm. Since this formation reaction of Pd NPs is a stoichiometric redox reaction between Pd(II) ions and the ntb units of the host ($Pd^{II} : ntb^{3-}$ = 1 : 2), a maximum of 9.05 wt% of Pd NPs can be formed if all of the ntb^{3-} units in the host are oxidized with palladium(II) ions. The PXRD pattern was retained intact even after the formation of Pd NPs that are larger than the channel size. This can be explained by the small volume ratio of Pd NPs produced *versus* the framework skeleton: even if all 3 wt% Pd NPs destroyed the framework, a maximum of 0.7% by volume of the framework skeleton could be destroyed according to the calculation.

This synthetic method for fabrication of M-NPs in PCPs *via* autoredox reaction has superior advantages such as neither a reducing agent nor a capping ligand is necessary, and the bare (naked) M-NPs are incorporated in porous host solids, which could be the leading candidates for heterogeneous catalysts as well as gas storage materials. Furthermore, the amount of M-NPs fabricated in PCPs can be controlled by the immersion time of the solid in metal ion solution and the concentration of the metal salts. The redox reaction can provide a 100% stoichiometric product. Although the resulting M-NPs often have larger diameters than the aperture size of the MOFs, the original structures of the frameworks are retained. The disadvantage is that the host solid should be oxidized and thus counter anions should be included in the pores, which reduces the surface area that is important for adsorption of gases and adsorbates.

Recently, it has been reported that when Rb-CD MOF and Cs-CD-MOF (CD = γ-cyclodextrin), which contain OH^- counter ions, were immersed in an acetonitrile solution of $AgNO_3$ and $HAuCl_4$, respectively, Ag NPs of 2.0 nm size and Au NPs of 3–4 nm size were formed.[30] In these cases, OH^- counter ions included in the frameworks either alone or cooperatively with the cyclodextrin units reduce the metal salt precursors to their
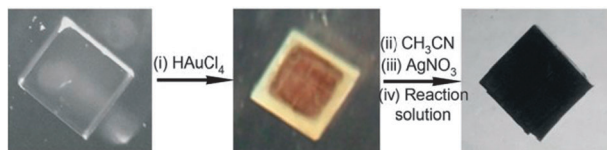
Fig. 4 Optical images of Rb-CD-MOF first loaded with Au NPs in the core region, and then with Ag NPs in the shell region. Reprinted with permission from ref. 30.

respective NPs. While Ag NPs were deposited throughout the entire MOF crystal, Au NPs were located predominantly in the core of the crystal. The amount of deposited M-NPs increases upon either increasing the time of soaking or increasing the concentration of the metal precursors. By combination of the deposition modes of Ag and Au, a core–shell NPs@CD-MOF was also synthesized. By immersion of MOF crystals first in HAuCl$_4$ solution, a core of Au NPs (>90%) was prepared, which was washed with acetonitrile and then immersed in AgNO$_3$ solution to deposit Ag NPs (>90%) in the shell region. The relative dimensions of the Ag-rich and the Au-rich regions could be adjusted by changing the core size, as shown in Fig. 4. Although the reduction of metal salts proceeds much faster in MeOH than in MeCN, MeOH could not be used because it caused degradation of the MOF scaffolds.

2.2 Chemical vapor deposition of organometallic compounds followed by hydrogenolysis

Chemical vapor deposition (CVD) of volatile organometallic precursors has been used for preparation of the metallic or metal oxide thin film on two-dimensional supports. This technique, however, has been applied not only to the "flat surface"[31] but also to the "internal surface" of the porous materials[32] to prepare the nanocomposite materials including metal complexes or metal clusters. In this technique, a dried MOF and a volatile metal precursor are placed in two separate glass vials in a Schlenk tube. The tube is evacuated, sealed, and kept at proper temperature depending on the vapor pressure of the metal precursor under static vacuum (1 Pa). Upon infiltration of the metal precursor into the MOF, the crystal colors of the MOF would be changed. When hydrogenolysis of the composite material is carried out to reduce the metal precursor, M-NPs incorporated in the MOF are generated.[33–35]

As shown in Fig. 5, various organometallic complexes that have appropriate sizes to enter into the cavities of the MOFs were used as precursors for CVD. When the vapor of $[(\eta^5\text{-}C_5H_5)Pd(\eta^3\text{-}C_3H_5)]$ (**A**),
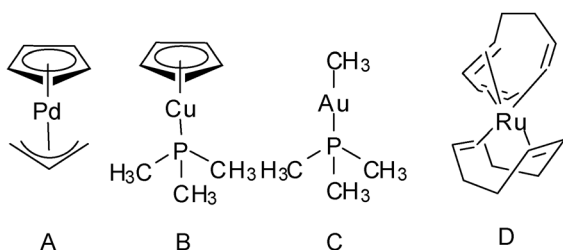
$[(\eta^5\text{-}C_5H_5)Cu(PMe_3)]$ (**B**), and $[(CH_3)Au(PMe_3)]$ (**C**), respectively, was introduced into MOF-5 that has a pore diameter of 8 Å, under static vacuum (1 Pa) at room temperature, metal precursors were embedded into MOF-5, as characterized by PXRD, elemental analysis, IR spectra, and solid state ^{13}C magic-angle spinning nuclear magnetic resonance (MAS NMR) spectra.[33] When the resulting **A**@MOF-5, **B**@MOF-5, and **C**@MOF-5 were treated with H$_2$ stream at the temperatures of hydrogenolysis (Pd for 23 °C, Cu for 150 °C, and Au for 190 °C), the "naked" metal-nanoclusters were formed. The sizes of the resulting M-NPs were 1.4 ± 0.1 nm for Pd@MOF-5, 3–4 nm for Cu@MOF-5, and 5–20 nm for Au@MOF-5. The polydispersity of Au NPs was explained by the high mobility of reduced Au nuclei in the open MOF-5 structure. In the PXRD pattern of Pd@MOF-5, characteristic peaks of the MOF-5 framework were significantly reduced, but the gas sorption data afforded a Langmuir surface area of 1600 m^2 g^{-1}, indicating that the framework of Pd@MOF-5 was still highly porous. In addition, instead of thermally induced hydrogenolysis, UV photolysis of the metal precursor infiltrated in MOF-5 was carried out by using a high pressure Hg lamp, which alternatively generated very small Pd and Cu NPs (1–2 nm) in the MOF-5 under much milder conditions.

Similarly, a Ru precursor, [Ru(cod)(cot)] (**D**, cod = 1,5-cyclooctadiene, cot = 1,3,5-cyclooctatriene), was loaded into MOF-5 by the CVD method.[34a] The homogeneous distribution of **D** in the MOF-5 framework was ascertained by a cross sectional photo as well as TEM images of **D**@MOF-5 crystals. The PXRD of **D**@MOF-5 showed the intact host structure even after inclusion of volatile Ru precursor **D**. Subsequent hydrogenolysis of the adsorbed **D** yielded Ru NPs of size 1.5–1.7 nm embedded in the MOF.[34a] In the hydrogenolysis reaction, mild conditions such as 25 °C for 30 min did not lead to the quantitative formation of Ru NPs. ^{13}C MAS NMR spectra indicated that hydrogenolysis of the cot ligand in **D** occurred prior to that of the cod ligand. The partially hydrogenated precursor **D** was converted to a [(cod)Ru(0)] fragment, and the Ru(0) atom formed a new coordination bond with a benzene ring of terephthalate in the host framework. Therefore, hydrogenolysis under mild conditions at 25 °C could not generate M-NPs. To obtain Ru@MOF-5 from **D**@MOF-5 quantitatively, the hydrogenolysis should be conducted under 3 bar H$_2$ at 150 °C for a longer period of time, 48 h. Quantitative hydrogenolysis of **D** and removal of all volatile byproducts from MOF-5 were confirmed by ^{13}C MAS NMR and FT-IR spectra. After complete decomposition of the Ru precursor **D**, the material Ru NPs@MOF-5 was obtained. In addition, this method was used to prepare Ni NPs in a mesoporous MOF, MesMOF-1 (Tb$_{16}$(TATB)$_{16}$, TATB = triazine-1,3,5-tribenzoate) (Fig. 6).[34c] After gas-phase loading of nickelocene in MesMOF-1, the sample was treated with hydrogen gas at 95 °C for 5 h, which yielded cyclopentane and Ni NPs included in MesMOF-1. When the residual cyclopentane molecules were removed by washing with methanol, Ni NPs@MesMOF-1 resulted. Depending on the loading time of the precursor, the amount of Ni NPs fabricated in MesMOF-s could be controlled.

This CVD method was also employed for the preparation of bimetallic nanoparticles such as FePt, PdPt, and RuPt in a MOF
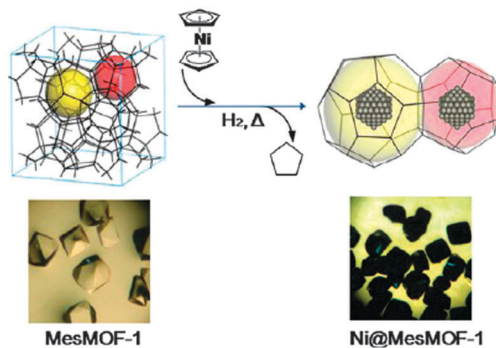

Fig. 5 Organometallic precursors for chemical vapor deposition.

Fig. 6 Preparation of Ni@MesMOF-1. Reprinted with permission from ref. 34c.

by loading MOF-5 with a combination of two different metal–organic CVD precursors.[35] In a Schlenk tube, dry MOF-5 and two metal precursors were placed, and the tube was evacuated (10^{-3} mbar), sealed, and kept at room temperature for several hours. The simultaneous loading of two different metal precursors in MOF-5 was verified by ^{13}C MAS NMR spectroscopy, PXRD and elemental/AAS (atomic absorption spectroscopy) analyses. After hydrogen treatment, the composite material of MOF-5 incorporating a bimetallic nanoalloy was obtained. In this reaction, the selection of proper temperature for hydrogenolysis is important, because if mild conditions are applied to avoid decomposition of the host framework MOF-5, both precursors could not be reduced to bimetallic alloy nanoparticles. When harsh conditions were applied to achieve quantitative co-hydrogenolysis of the precursors, the hydrogenation of bdc linkers in MOF-5 occurred to yield *cis/trans*-1,4-cyclohexane dicarboxylic acid.

2.3 Chemical vapor deposition of an organometallic compound followed by thermal decomposition

Recently Suh's group reported that they fabricated hexagonal-disk shaped magnesium nanocrystals (Mg NCs) within a MOF by chemical vapor deposition followed by simple thermal decomposition without a hydrogenolysis step.[21] They deposited the vapor of bis-cyclopentadienyl magnesium (MgCp$_2$) in SNU-90′ at 80 °C. The resulting MgCp$_2$@SNU-90′ was thermally decomposed at 200 °C under an argon atmosphere, followed by removal of the organic by-products by evacuation. The reaction resulted in hexagonal-disk shaped Mg NCs embedded in SNU-90′. The absence of the organic traces for the decomposed bis-cyclopentadienyl was checked with the NMR spectra. The amount of Mg NCs embedded in the MOF could be controlled by the reaction conditions during the chemical vapor deposition of Mg(Cp)$_2$, such as length of the deposition time and whether or not the prevacuum state was maintained in the reaction bottle. The Mg nano disk had the diagonal length and the thickness of a hexagon, average 60 ± 18 nm and average 37 ± 12 nm, respectively.

Even though Mg NCs were much bigger than the channel size (12.9 Å × 9.6 Å) of the MOF, they were embedded inside the channels of the MOF as confirmed by TEM and electron tomography (Fig. 7). The powder X-ray diffraction (PXRD) patterns showed that the structure of SNU-90′ was maintained
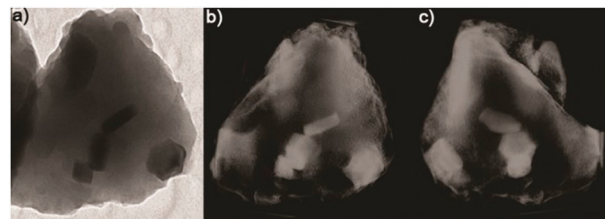

Fig. 7 TEM and electron tomography images of Mg@SNU-90′. (a) TEM image. (b) and (c) Tomographically reconstructed images of Mg NCs embedded in SNU-90′ at different angles. Reprinted with permission from ref. 21.

even after the formation of Mg NCs. When the Mg@MOF was exposed to air for 2 days, the PXRD pattern showed the peaks corresponding to MgO, with retention of the framework structure of SNU-90′.

2.4 Immersion of MOFs in metal salt solutions followed by reduction

This approach is based on the solution-phase technique. A porous support is immersed in the solution of a metal precursor. The metal precursor is mostly metal salt such as metal nitrate and chloride, and is completely dissolved in an organic solvent or sometimes in water. When the dried porous solid is soaked in the metal ion solution, the metal ions are infiltrated into the empty pores. The metal precursors should be carefully selected by considering the size of pores or channels of the MOF. After removal of the guest solvent molecules included in the host framework, the metal ions impregnated in the solid support are reduced by a reducing agent, typically H$_2$ gas, to obtain M-NPs embedded in the MOF.

Recently Latroche *et al.* adopted this technique to prepare Pd NPs (2.0 nm) embedded in a MOF, MIL-100(Al) (MIL represents Materials of Institut Lavoisier).[15] MIL-100(Al) has the 3D structure of cubic zeolitic MTN topology, with two types of large cavities (effective internal diameters: 2.1 and 2.5 nm, respectively), having a smaller window opening of size 8.7 Å (Fig. 8). Therefore, MIL-100(Al) is accessible by [PdCl$_4$]$^{2-}$ whose longest edge is 5.7 Å. MIL-100(Al) was immersed in a 10% (v/v) aqueous HCl solution of H$_2$PdCl$_4$, and then the impregnated Pd complex was reduced with Ar–H$_2$ flow at 553 K for 6 h. The Pd NPs impregnation in MIL-100(Al) was evidenced by PXRD, inductively coupled plasma (ICP), and transmission electron microscopy (TEM) images. In the PXRD of Pd@MIL-100(Al), additional peaks to those of the host framework were found at 40.2°, 46.5°, 68.2°, and 81.1°, which corresponded to an α phase of a Pd cubic cell (*Fm*$\bar{3}$*m*). Based on the N$_2$ adsorption–desorption isotherms for MIL-100(Al) and Pd@MIL-100(Al), it was revealed that the BET surface area and the total pore volume of the framework were greatly reduced upon loading of Pd NPs in MIL-100(Al), from 1200 to 380 m^2 g^{-1} and from 0.65 to 0.33 cm^3 g^{-1}, respectively. This indicates that insertion of Pd NPs alters the pore structure of MIL-100(Al).

In particular, the incipient wetness method, which is also called the capillary impregnation or dry impregnation method, is one of the impregnation techniques that have been developed to

1812 | *Chem. Soc. Rev.*, 2013, **42**, 1807–1824

This journal is © The Royal Society of Chemistry 2013
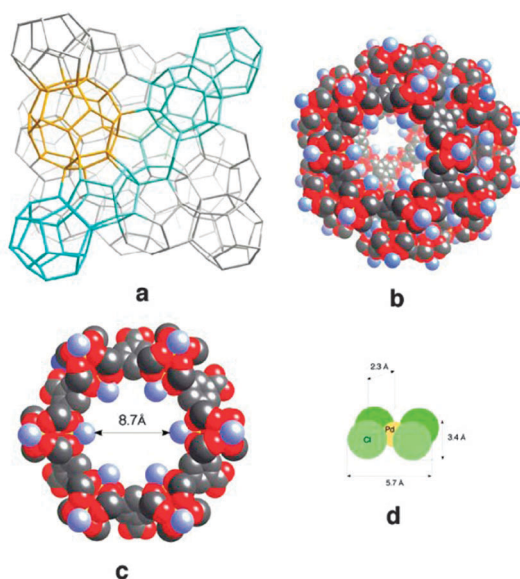
Fig. 8 (a) The MTN topology of MIL-100(Al): large cages are in yellow and small ones in turquoise. (b) Space-filling perspective view of the large cage of MIL-100(Al): carbon in gray, oxygen in red, terminal groups (water or OH) in pale blue. (c) Space-filling representation of the hexagonal window of the large cage (the same color codes as in panel b). (d) Size comparison of the $[PdCl_4]$ anion at the same scale. Reprinted with permission from ref. 15.

prepare heterogeneous catalysts. The solution of metal precursor, whose volume is the same as the total pore volume of the support, is added to the dried solid support. When the guest-free solid support and a definite amount of solution are mixed, capillary force leads the solution to fill the pores. Therefore, the incipient wetness method is called capillary impregnation or dry impregnation. The successive reduction reaction of the metal precursor generates M-NPs in the support. The proper choice of solvents, for example, water, polar, or nonpolar organic solvent, should be made based on the surface nature of the porous solid, so that the solution can be comfortably introduced into the pores of the porous solid. In this method, the loading amounts of metal are feasibly controllable by varying the concentrations of the precursor solution, and accordingly, the maximum loading amount is restricted by the solubility of the metal precursor in the solvent.[16]

Kaskel *et al.* introduced a similar method to embed Pd NPs in MOF-5.[36] The total volume of chloroform solution of $[Pd(acac)_2]$ (acac = acetylacetonate) was calculated from the pore volume of the desolvated MOF-5 (1.18 cc g^{-1}), and the exact amount of precursor solution was infiltrated into the empty space of MOF-5. The thermal (150 or 200 °C under vacuum) or hydrogen treatment (150 or 200 °C in H$_2$ flow) was conducted subsequently to reduce metal precursors to M-NPs. Various reduction conditions were applied to optimize the performance of the catalyst. During this hydrogen reduction, the benzene-1,4-dicarboxylate ligand was not hydrogenated as evidenced by ^{1}H and ^{13}C NMR spectra of Pd@MOF-5. The PXRD patterns measured after inclusion of Pd(acac)$_2$ and then reduction to Pd NPs in MOF-5 indicated that the 3D structure of MOF-5 remained unchanged.

Xu *et al.* have reported the fabrication of Pt-NPs in MIL-101(Cr) by using a "double solvent" method in order to avoid the aggregation of M-NPs on the external surface of the MOF.[37] The method involves immersion of a MOF in the metal salt solution, but it employs two different solvents, a hydrophilic solvent (water) and a hydrophobic solvent (hexane). The method minimizes the deposition of the precursor compound on the outer surface of the MOF. In the experimental process, the activated MOF was suspended in a large amount of dry *n*-hexane, to which was added the metal precursor (H$_2$PtCl$_6$) dissolved in water with a volume set equal to or less than the pore volume of the adsorbent (MIL-101). Because MIL-101(Cr) has a much larger inner surface area with hydrophilic character than the outer surface, the small amount of aqueous H$_2$PtCl$_6$ (equal to or less than pore volume) was readily incorporated into the pores by capillary force, which greatly minimizes the deposition of the precursor on the outer surface. After loading the precursor, the samples were treated with H$_2$–He stream at 200 °C for 5 h. By varying the concentration of the Pt precursor, various amounts of Pt NPs were loaded in MIL-101. The average size of Pt NPs formed was 1.8 ± 0.2 nm. The Pt@MIL-101 showed catalytic performance in various reactions such as ammonia borane hydrolysis, ammonia borane thermal dehydrogenation, and CO oxidation.

2.5 Immersion of MOFs in metal salt solutions followed by UV irradiation

It is possible to deposit M-NPs in the core of MOF crystallites by photochemical generation. For example, Ag@MOF-5 was prepared by photo catalytic reduction of Ag(I). When an ethanol solution of AgNO$_3$ was stirred in the presence of MOF-5 under UV irradiation, Ag NPs were formed in MOF-5.[38] The formation of Ag NPs in MOF-5 was evidenced by the color change of MOF-5 from white powder to dark brown-black. Similarly to the other observations, the PXRD pattern of Ag@MOF-5 indicated that MOF-5 structure was retained even after the formation of Ag NPs. The main advantage of the photochemical generation of M-NPs is the spatial resolution that can be achieved by using a light beam to effect the reduction leading to metallic particles. That is, by using this method, it may be possible to fabricate M-NPs in a specific part of the MOF crystal leaving the other part of the crystal without NPs. The photo catalytic reduction may be applied to prepare other noble metals. However, this photo catalytic reduction procedure is not generally applicable to all MOFs. This can be applied only to semiconducting MOFs. In contrast to the case of MOF-5, when MIL-53(Al) that contains the same terephthalate ligand but with Al^{3+} as a metal ion was used as a solid support, Ag NPs were not produced by similar photo irradiation. This is because MOF-5 is a semiconductor that is able to effect the photo catalytic reduction of noble metal ions, while MIL-53(Al) is not a semiconductor.

2.6 Impregnation of a metal salt in a photoactive MOF followed by visible light irradiation

Recently Lin *et al.* constructed photoactive MOFs that have the ability to generate Pt NPs by triethylamine (TEA)-mediated photoreduction.[18] The MOFs were prepared *via* a solvothermal reaction of
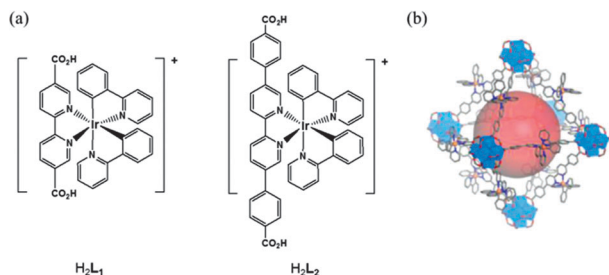
Fig. 9 (a) [Ir(ppy)₂(bpy)]⁺-derived dicarboxylic acids H₂L₁ and H₂L₂. (b) The crystal structure of the photoactive MOF constructed from H₂L₂ and Zr⁴⁺. Reprinted with permission from ref. 18.

$[Ir(ppy)_2(bpy)]^+$-derived dicarboxylic acids, H₂L₁ (L₁ = 2,2′-bipyridine-5,5′-dicarboxylate) and H₂L₂ (L₂ = 2,2′-bipyridine-5,5′-dibenzoate; ppy = 2-phenyl-pyridine; bpy = 2,2′-bipyridine) (Fig. 9a) with Zr⁴⁺. The resultant MOFs, Zr₆(μ₃-O)₄(μ₃-OH)₄(bpdc)₅.₉₄(L₁)₀.₀₆ (6) and Zr₆(μ₃-O)₄(μ₃-OH)₄(L₂)₆·64DMF (7), adopted the face centred cubic topology (fcu in classification of the Reticular Chemistry Structure Resource, available at http://rcsr.anu.edu.au) by connecting the Zr₆(μ₃-O)₄(μ₃-OH)₄(carboxylate)₁₂ secondary building units with the linear linker L₁ and L₂, respectively (Fig. 9b). The [Irᴵᴵᴵ(ppy)₂(bpy)]⁺ moiety in the MOFs can be excited by visible light to an excited state of [Irᴵᴵᴵ(ppy)₂(bpy)]⁺*, which exhibits phosphorescence emission through an intersystem crossing. A mixture of K₂PtCl₄ and the MOF powder in a mixed solvent of tetrahydrofuran (THF)–TEA–H₂O was degassed and then irradiated with visible light from a 450 W Xe-lamp with a 420 nm cut-off filter. TEA reductively quenches the photoexcited [Irᴵᴵᴵ(ppy)₂(bpy)]⁺* to generate the reduced radical, [Irᴵᴵᴵ(ppy)₂(bpy•⁻)]], which reduces K₂PtCl₄ to form Pt nanoparticles within the host framework. Pt NPs with diameters of 2–3 nm in 6 and 5–6 nm in 7 were generated by an *in situ* photoreduction of K₂PtCl₄. Furthermore, the radicals can transfer electrons to the Pt NPs to reduce protons in water for hydrogen production. The PXRD pattern of Pt@MOF indicated that the framework structure was maintained even after loading of the Pt NPs.

2.7 Microwave irradiation on a MOF and metal precursor mixture

Although the reports existing so far are extremely rare, M-NPs can be fabricated on a MOF by microwave irradiation. By using the microwave-irradiation heating method, the activation of the pores of MIL-101 and the rapid chemical reduction of metal precursors were simultaneously performed in the presence of a reducing agent, which resulted in the formation of small Pd, Cu, and Pd–Cu nanoparticles of 2–3 nm within the pores and larger particles of 4–6 nm on the surface of the MIL-101 crystals.[20]

## 2.8 Grinding solid precursors with MOFs followed by hydrogenation

The solid grinding method is also an effective and facile route to fabricate M-NPs into porous materials.[17,39,40] Activated metal–organic frameworks which have accessible pore openings are

ground together with volatile organometallic precursors in a mortar for several minutes at room temperature without using organic solvents. During grinding, the volatile precursor is sublimated and its vapor diffuses rapidly through the cavities of the MOF, which results in well-distributed deposition of the precursor. The metal precursor embedded in the porous MOF is treated with H₂ gas at high temperature, which produces very small M-NPs.

Haruta and Xu *et al.* reported several heterogeneous catalysts prepared by simple grinding of [Au(acac)(CH₃)₂] (acac = acetylacetonate) and porous MOFs such as MOF-5, HKUST, ZIF-8, MIL-53(Al), and CPL-2.[17,39,40] Au NPs of size *ca.* 2 nm with small standard deviations, 2.2 ± 0.3 nm and 1.5 ± 0.7 nm, were fabricated in CPL-2 and MIL-53(Al), respectively. This is contrary to those obtained by a CVD method, which results in 3.0 ± 1.9 nm NPs with wider standard deviation in CPL-2.[41] Specific surface area of Au@CPL-2 prepared by the solid grinding method was reduced to 64 m² g⁻¹ from 500 m² g⁻¹ of as-synthesized CPL-2. This is attributed to the pore blocking by Au NPs as well as partial degradation of the porous structure. However, the PXRD pattern of Au@CPL-2 was the same as that of CPL-2, indicating that a large part of the host framework was still intact. The nanocomposites of small Au NPs and ZIF-8 show catalytic activity toward CO oxidation reaction to produce CO₂.[39]

2.9 Encapsulation of presynthesized metal nanoparticles in MOFs

Presynthesized metal NPs that are capped by stabilizing agents can be encapsulated in MOFs by introducing NPs into a synthetic solution containing molecular building blocks for MOFs. When individually capped-NPs are encapsulated in MOFs, the size of NPs can be easily controlled, and agglomeration of nanoparticles can be restricted in the host framework. Hupp and Huo *et al.* reported encapsulation of the PVP (polyvinylpyrrolidone)-capped nanomaterials with various sizes, shapes, and compositions in a zeolitic imidazolate framework, ZIF-8 (Fig. 10).[42] PVP has been widely used in the synthesis of various nanomaterials to control
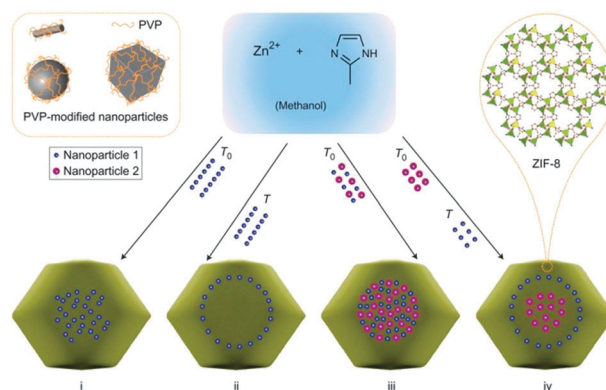
Fig. 10 Scheme of the controlled encapsulation of nanoparticles in ZIF-8 crystals. Through surface modification with surfactant PVP, nanoparticles of various sizes, shapes and compositions can be encapsulated in a well-dispersed fashion in ZIF-8 crystals, which formed by the assembly of zinc ions and imidazolate ligands. Reprinted with permission from ref. 42.

the size and shape as well as to stabilize them in polar solvents. By mixing PVP-capped Au NPs with a methanolic solution of zinc nitrate and 2-methylimidazole, Au@ZIF-8 was isolated by centrifugation. After isolation, the supernatant did not contain Au NPs, implying that almost all NPs were encapsulated in ZIF-8. This strategy was successfully extended to other nano-materials such as Pt, CdTe, Fe_3O_4 and lanthanide-doped $NaYF_4$ nanoparticles, and Ag cubes, polystyrene spheres, β-FeOOH rods and lanthanide-doped $NaYF_4$ rods, whose surfaces were modified by PVP.[42]

3. Characterization of nanocomposites

Because M-NPs@MOFs is a complex system of organic–inorganic hybrid material, various analytical and spectroscopic tools should be employed for the characterization. During and/or after synthesis of the nanocomposites, both resultant nano-particles and supporting MOFs should be carefully analyzed to explain the formation mechanism. The objects and tools for the characterization are listed below.

(1) Deposition of metal precursors within porous MOFs: inductively coupled plasma (ICP) spectroscopy, infrared (IR) spectroscopy, magic angle spinning (MAS) nuclear magnetic resonance (NMR) spectroscopy, elemental analysis, X-ray photo-electron spectroscopy (XPS).

(2) Morphology, size, distribution, and coordination environment of M-NPs: transmission electron microscopy (TEM), energy dispersive spectroscopy (EDS), extended X-ray absorption fine structure (EXAFS), ICP.

(3) Structural changes of MOFs after loading M-NPs: powder X-ray diffraction (PXRD) data.

(4) Features of nanocomposites: electron paramagnetic reso-nance (EPR), TEM, EDS, PXRD, ICP, BET measurement, XPS.

Loading of a volatile organometallic precursor, [Ru(cod)(cot)] (D, Fig. 5) (cod = 1,5-cyclooctadiene, cot = 1,3,5-cyclooctatriene), into MOF-5 by a CVD method was evidenced by solid state ^{13}C MAS NMR spectroscopy.[34a] As shown in Fig. 11, the carbon resonance signals indicated that the precursor D was included in MOF-5, and the nature of D was unchanged even after intercalation. Precursor D included in MOF-5 exhibited peaks with the chemical shifts very similar to those measured for pristine D in C_6D_6 rather than to those in the solid state. This means that D included in MOF-5 has high mobility, and behaves like being in the solution. The ^{13}C MAS NMR spectrum of D@MOF-5 after hydrogenolysis revealed that depending on the reaction temperature, degree of hydrogenation of D was varied. Under mild reduction conditions (25 °C, 30 min), Ru was still coordinated with the cot ligand, but it dissociated cod to interact with the bdc linker. Under harsh conditions (3 bar of H_2, 150 °C, 48 h), D@MOF-5 was quantitatively hydrogenized to yield Ru@MOF-5. In this case, MAS-NMR spectroscopy was used as a very powerful tool to elucidate the mechanism of formation of M-NPs in porous MOFs.

Transmission electron microscopy (TEM) is the most common and important technique to elucidate morphology, size, crystal structure, dispersity, and distribution of M-NPs within MOFs.
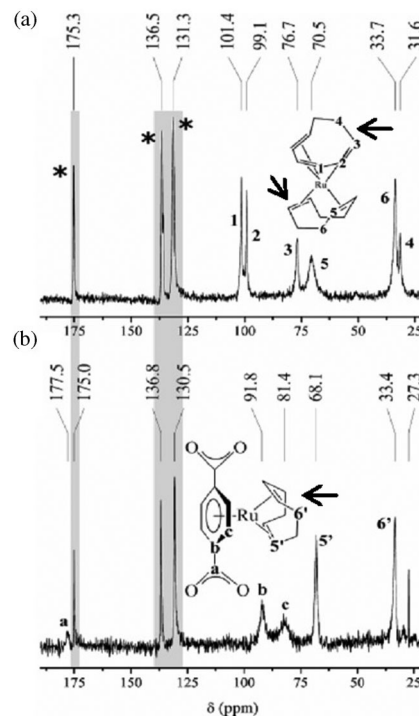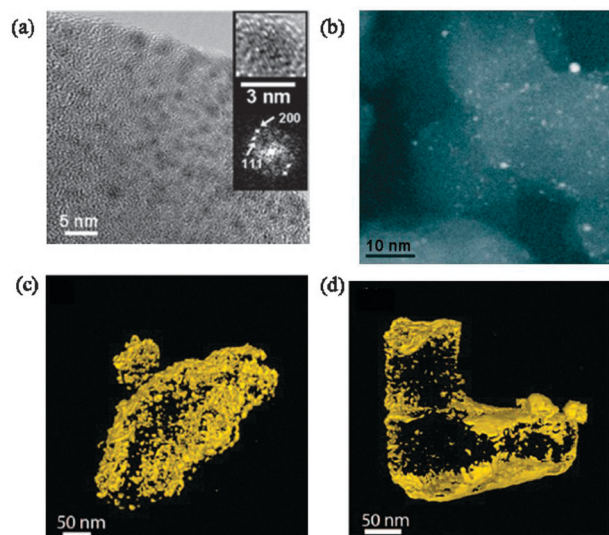

Fig. 11 ^{13}C MAS NMR spectra of **D**@MOF-5 before (a) and after (b) hydrogenolysis at 1 cc min^{-1} with H_2 at 25 °C for 30 min. Signals of MOF-5 are shaded. The carbon signals of MOF are marked with asterisks. Reprinted with permission from ref. 34a.

In addition to this, various tools such as high-resolution TEM (HR-TEM), selected area electron diffraction (SAED), high-angle annular dark-field scanning transmission electron microscopy (HAADF-STEM), tomography, energy dispersive spectroscopy (EDS), and electron energy loss spectroscopy (EELS) mapping can be utilized complementarily to explain the formation of M-NPs in MOFs clearly.

As shown in Fig. 12a, SAED combined with HR-TEM measure-ment for Pd NPs@**4** indicated that the autoredox reaction between the included Pd^{II} ions and redox active PCP **4** yielded 2.9 ± 0.4 nm Pd NPs, which had a face-centered cubic (fcc) structure with a $d(111)$ spacing of 0.23 nm. Small metal NPs less than 2 nm are more clearly seen in HAADF-STEM.[27] In Fig. 12b, small Au NPs with a mean diameter of 1.5 nm incorporated in MIL-53(Al) are clearly seen in the dark-field image obtained in STEM mode.[17] Although TEM is an essential tool to examine nano-sized materials, it has a limitation of providing only 2D information projected along the beam direction. In addition, it was demonstrated that rapid TEM-induced degradation of MOFs led to agglomeration of the initially formed small metal clusters, in particular Ag_3 clusters, into the stable and easily imaged bigger particles.[43]

As shown in Table 1, there are many reports indicating that M-NPs larger than the pore size of the MOF were formed. Therefore, the location of M-NPs deposited on MOFs has been a controversial issue. However, TEM cannot provide explicit solution to the dispute whether the M-NPs locate inside of the pores or only on the surface of the MOF. To address this issue,

This journal is © The Royal Society of Chemistry 2013

Chem. Soc. Rev., 2013, **42**, 1807–1824 | **1815**

Fig. 12 (a) HR-TEM image and SAED for Pd NPs@**4**. (b) HAADF-STEM image of Au NPs@MIL-53(Al). Tomographically reconstructed images of (c) Pd NPs and (d) Ru NPs in MOF-5. Reprinted with permission from ref. 27 (a), ref. 17 (b), and ref. 44 (c and d).

the tomographic reconstruction of TEM images, which are taken using a 2° interval through the use of a penetrating e-beam, should be carried out to give 3D information. The electron tomography performed for Pd@MOF-5 and Ru@MOF-5 verified the position and distribution of the particles within the framework.[34a] As shown in Fig. 12c and d, the tomography images revealed that introduction of different kinds of metal precursors followed by reduction afforded various degrees of penetration and dispersion of the nanoparticles. The Pd NPs in Pd@MOF-5 had sizes ranging from 1 to 5 nm as evidenced by bright field TEM images, and the electron tomography indicated that Pd NPs with 1–3 nm size were distributed within the MOF-5 whereas larger particles/agglomerates were mostly located at the surface of MOF-5 (Fig. 12c).[44] In the TEM images of Ru@MOF-5, the particles seemed to be dispersed within MOF-5, but 3D tomographic reconstruction of Ru@MOF-5 revealed that particles were penetrated to only 20 nm depth of the host frameworks, and located at or close to the surface of the MOF-5 (Fig. 12d).[44]

The positions of Ag clusters incorporated in MOF-508 were also proved by tomography, which indicated that Ag clusters are permeated in the entire MOF matrix.[43] In this report, the authors claimed that the TEM electron beam rapidly (within several seconds) damages the framework structure of the soft material MOF, which facilitated aggregation of Ag nanoparticles resulting in NPs larger than the pore size of the MOF. To minimize this effect, during TEM measurement the specimen was cooled to *ca.* 100 K, and the beam was defocused. By comparison with TEM images of Ag@MIL-68(In) before and after e-beam damage, it was revealed that the beam significantly affected agglomeration of Ag NPs embedded in the MOF (Fig. 13). Even though the TEM technique was not appropriate to characterize as-synthesized Ag NPs, EPR spectroscopy confirmed the formation of Ag₃ clusters, which were small enough to be embedded in pores of MOFs.

FT-IR analysis also indicated that the MOF provided a large kinetic barrier toward crystallization.

The possible structural changes of MOFs before and after loading M-NPs were monitored by PXRD patterns. As shown in Fig. 14, by the comparison of PXRD patterns, it was revealed that the original structure of **1** was maintained even after Ag NPs were generated in PCP **1** by the autoredox reaction between Ag(I) ions and Ni(II) species incorporated in **1**.[24] However, when the reaction time was prolonged, the PXRD pattern became weaker and broader, suggesting that the original host structure could be destroyed. During the autoredox reaction, the oxidation states of metal precursors as well as the metal ions in the host framework were studied by EPR and XPS analyses.[14,24–27]

EPR spectroscopy and XPS are also used to verify the M-NPs incorporated in MOFs. When a redox active PCP, [(NiL₂)₂(bptc)]·2H₂O (**2**), was immersed in an EtOH solution of NaAuCl₄·2H₂O for several min at room temperature, *ca.* 2 nm size Au NPs were formed in **2**.[25] The EPR spectrum measured for Au NPs@**2** showed the anisotropic signals at $g_\perp = 2.177$ and $g_\parallel = 2.026$, clearly indicating tetragonally distorted Ni(III) species (Fig. 15a). The XPS data (Fig. 15b) showed that Au(0) and Ni(III) species coexisted in the nanocomposites. These indicated that the Ni(II) species incorporated in **2** were oxidized to Ni(III) species, and simultaneously Au(III) was reduced to Au(0) atoms, which aggregated into Au NPs.

Although TEM is an effective technique to observe the morphology and size of metallic NPs, it has the limitation of resolution, and well-dispersed metal clusters less than 1 nm size cannot be distinguished by HAADF-STEM images as well as by bright-field TEM images. As shown in Fig. 16, EXAFS can precisely tell the size, coordination environment, and chemical form of very small metal clusters. By the solid-grinding method, Au clusters smaller than 1 nm were successfully intercalated in a porous Cd-MOF, but the ultrafine Au clusters could not be detected by TEM.[40] However, Au L$_{\mathrm{III}}$-edge EXAFS revealed the presence of Au⁰ and ultrafine gold clusters with the average atom number of 2.5. In addition, from this analysis, kinds of bonds between Au atoms and others and the coordination number of Au atoms could be determined. It was revealed that Au atoms interacted with F and O atoms of the host framework.

4. Important issues for M-NPs@MOF

On characterization of M-NPs@MOF, several important issues should be addressed such as (1) size control of M-NPs in MOFs, (2) size of M-NPs *vs.* cavity size of MOF, (3) localized destruction of the framework upon loading M-NPs, and (4) location of M-NPs in MOFs. Although these issues are related to each other, here we discuss them separately.

4.1 Size control of M-NPs: size of M-NPs *vs.* cavity size of MOF

Size of M-NPs loaded in the MOFs often cannot be easily controlled even under controlled experimental conditions. In the case of simple immersion of redox active PCPs in the metal salt solutions, the average size of the resulting M-NPs is independent of immersion time, concentration of the metal

1816 | *Chem. Soc. Rev.*, 2013, **42**, 1807–1824

This journal is © The Royal Society of Chemistry 2013

Table 1 Preparation method, particles size, and application of various M-NP@MOFs

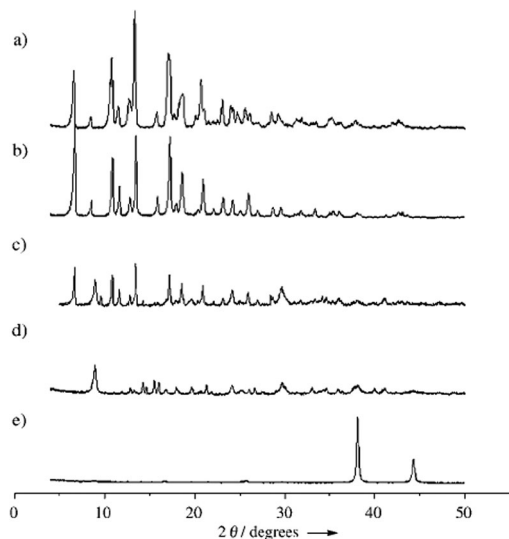| Section	Metal precursor[a] (loading amount, wt%)	MOF[b] (pore size, Å)	Preparation method (solvent)	Reduction method	Metal size (nm)	Application	Ref.
2.1	$AgNO_3$	$[Ni(C_{10}H_{26}N_6)]_3(bpdc)_3$ (7.3)	Impregnation (methanol)	Redox-active Ni^{II} macrocycle	3	—	24[c]
	$AgNO_3$	$[Ni(cyclam)]_2[bptc]$	Impregnation (ethanol)	Redox-active Ni^{II} macrocycle	3.7 ± 0.4	—	25[c]
	$AgNO_3$ $HAuCl_4$	Cs-CD-MOF/ Rb-CD-MOF (8)	Impregnation (acetonitrile)	OH^- counter ions in MOF	(Ag, 2 0. ± 4) (Au, 3–4)	—	30
	$NaAuCl_4 \cdot 2H_2O$	$[Ni(cyclam)]_2[bptc]$	Impregnation (ethanol)	Redox-active Ni^{II} macrocycle	2	—	25
	$Pd(NO_3)_2$ (1.0 wt%)	$[Ni(cyclam)]_2(mtb)]$ (2.05)	Impregnation (acetonitrile)	Redox-active Ni^{II} macrocycle	2.0 ± 0.6	—	26[c]
	$Pd(NO_3)_2$ (5.0 wt%)	$[Ni(C_{20}H_{32}N_8)]_2[tcm]$ (4.5 × 2.1)	Impregnation (acetonitrile)	Redox-active Ni^{II} macrocycle	2.9 ± 0.4	—	27[c]
	$Pd(NO_3)_2 \cdot 2H_2O$ (3.2 wt%)	$[Zn_3(ntb)_2(EtOH)_2]$ (7.7)	Impregnation (acetonitrile)	Redox active MOF	3.0 ± 0.4	Hydrogen storage	14
2.2	$Au(CO)Cl$ (30 wt%)	ZIF-8/ZIF-90 (12)	Chemical vapor deposition	H_2, 2 bar, 100–130 °C	(ZIF-8) 3.2 ± 0.1 (ZIF-90) 1.4 ± 0.2	Oxidation of alcohols	34b[c]
	$(CH_3)Au(PMe_3)$ (48 wt%)	MOF-5	Chemical vapor deposition	H_2, 190 °C, 4 h	5–20	CO oxidation (inactive)	33
	$(\eta^5\text{-}C_5H_5)Cu(PMe_3)$ (13.8 wt%)	MOF-5	Chemical vapor deposition	H_2, 150 °C, 1 h	1–2	Methanol production from syngas	33
	$NiCp_2$	MesMOF-1 (1.5, 1.7)	Chemical vapor deposition	H_2, 95 °C, 5 h	—	Conversion of styrene to ethylbenzene	34c[c]
	$(\eta^5\text{-}C_5H_5)Pd(\eta^3\text{-}C_3H_5)$ (35.6 wt%)	MOF-5	Chemical vapor deposition	H_2, 23 °C, 30 min	1–2	Hydrogenation	33
	$Ru(cod)(cot)$ (18.7 wt%)	MOF-5	Chemical vapor deposition	H_2, 3 bar, 150 °C	1.5–1.7	Oxidation of alcohols, hydrogenation of benzene	34a[c]
2.3	$MgCp_2$ (10.6 wt%)	SNU-90 (12.9 × 9.6)	Chemical vapor deposition	Thermal decomposition	60 ± 18	Hydrogen storage	21
2.4	$HAuCl_4$ (0.47–0.52 wt%)	MIL-101 (30)	Impregnation (water)	H_2, 200 °C, 2 h	9.8 ± 3.4	Oxidation of alcohols	19
	H_2PdCl_4 (10 wt%)	MIL-100(Al) (8.7)	Impregnation (water)	H_2, 553 K	1.8 ± 0.4	Hydrogen storage	15
	$Pd(acac)_2$ (20.9 wt%)	MOF-5 (7)	Incipient wetness ($CHCl_3$)	H_2, 80 °C	40	—	16
	$Pd(acac)_2$ (1.04 wt%)	MOF-5	Incipient wetness impregnation ($CHCl_3$)	Vacuum heating (150–200 °C)/ H_2 (150–200 °C)	—	Hydrogen storage/ hydrogenation	36[c]
	H_2PtCl_6	MIL-101(Cr) (12, 16)	Impregnation (water–hexane)	H_2, 200 °C, 5 h	1.8 ± 0.2	Ammonia borane hydrolysis/ CO oxidation	37
2.5	$AgNO_3$	MOF-5	Impregnation (ethanol)	UV irradiation	—	—	38
2.6	K_2PtCl_4	$Zr_6(\mu_3\text{-}O)_4(\mu_3\text{-}OH)_4(bpdc)_{5.94}(L_1)_{0.06}$	Impregnation (THF–TEA–H_2O)	Photoreduction Xe-lamp	2–3		18
		$Zr_6(\mu_3\text{-}O)_4(\mu_3\text{-}OH)_4(L_2)_6 \cdot$ 64DMF (16)			5–6		18
2.7	$Pd(NO_3)_2$ (4.9 wt%)/ $Cu(NO_3)_2$ (2.0 wt%)	MIL-101 (30)	Impregnation (water)	Hydrazine with microwave irradiation	2–3, 4–6	CO oxidation	20
2.8	$Me_2Au(acac)$	CPL-1 (4 × 6)	Solid grinding	H_2 120 °C, 2 h	—	Catalyst: oxidation of alcohols	17
		CPL-2 (6 × 8)			2.2 ± 0.3		
		MIL-53(Al) (8.5 × 8.5)			1.5 ± 0.7		
		MOF-5 (15 × 15)			—		
		Cu-BTC (11 × 11)			—		
	$(CH_3)_2Au(acac)$	ZIF-8	Solid grinding	H_2, 230 °C, 2.5 h	3.4 ± 1.4	CO oxidation	39[c]
	$(CH_3)_2Au(acac)$ (1 wt%)	$[Cd_2(L)\cdot(H_2O)]\cdot0.5H_2O$	Solid grinding	H_2, 170 °C, 2 h	—	—	40
	5 wt% Pt supported on active carbon	MOF-5/IRMOF-8	Ground together	—	—	Hydrogen storage	47
2.9	Presynthesized M NPs M = Au, Pt, CdTe, Fe_3O_4, $NaYF_4$, Ag cubes, β-FeOOH	ZIF-8	Encapsulation of presynthesized metal nanoparticles	—	Au(13)/Pt (2.5, 3.3, 4.1)/ CdTe (2.8)/Fe_3O_4 (8)/ $NaYF_4$ (24)/Ag cubes (160)/β-FeOOH (22 × 160)	Catalyst, magnetic and optical material	42
Others	$AgNO_3$	Cu(BTC)/MOF-508/ MIL-68(In)	Impregnation (water–ethanol)	Ethanol	≤1	—	43[c]
	$HAuCl_4$ (0.47–0.52 wt%)	MIL-101 (30)		$NaBH_4$	2.3 ± 1.1/6.4 ± 2.6	Oxidation of alcohols	19

Table 1 (continued)

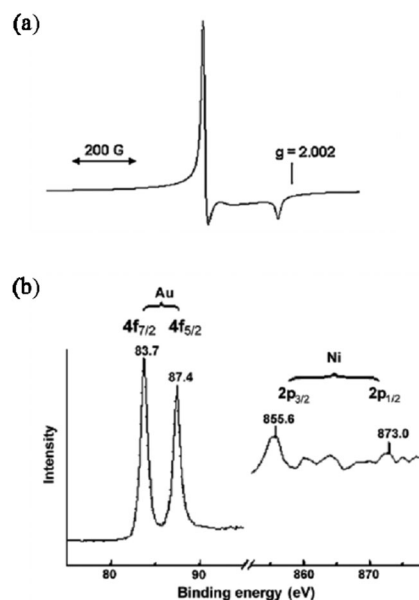| Section	Metal precursor[a] (loading amount, wt%)	MOF[b] (pore size, Å)	Preparation method (solvent)	Reduction method	Metal size (nm)	Application	Ref.
	Pd(η^5-C$_5$H$_5$)(η^3-C$_3$H$_5$) (35 wt%)	MOF-5 (7)	Colloidal deposition (water) Chemical vapor deposition	Photolysis UV light at RT	2.4 ± 0.2	—	16[c]
	[PdCl$_4$]$^{2-}$, [PtCl$_6$]$^{2-}$, [AuCl$_4$]$^-$	MIL-101(Cr) (12, 16)	Anion exchange	NaBH$_4$	2–4	Heck reaction	50
	RuCl$_3 \cdot$3H$_2$O (0.98 wt%)	La(1,3,5-BTC)$\cdot$6H$_2$O	Colloidal deposition (supercritical CO$_2$–methanol)	Methanol	2	Hydrogenation	23

[a] Metal precursor = NiCp$_2$: Cp = cyclopentadienyl/[Ru(cod)(cot)]: cod = 1,5-cyclooctadiene; cot = 1,3,5-cyclooctatriene/Pd(acac)$_2$: acac = acetyl-acetonate. [b] MOF = [Ni(C$_{10}$H$_{26}$N$_6$)]$_3$(bpdc)$_3$: bpdc = [Ni(cyclam)]$_2$[bptc]: cyclam = 1,4,8,11-tetraazacyclotetradecane; H$_4$bptc = 1,1'-biphenyl-2,2', 6,6'-tetracarboxylic acid/Cs-CD-MOF; Rb-CD-MOF: CD = cyclodextrin/[Ni(cyclam)]$_2$(mtb): mtb = methanetetrabenzoic acid/[Ni(C$_{20}$H$_{32}$N$_8$)]$_2$[tcm]: tcm = tetrakis[4-(carboxyphenyl)oxamethyl]-methane/[Zn$_3$(ntb)$_2$(EtOH)$_2$]: ntb = 4,4',4''-nitrilotrisbenzoate/ZIF-8: Zn(MeIM)$_2$; IM = imidazolate/ZIF-90: Zn(ICA)$_2$; ICA = imidazolate-2-carboxyaldehyde/MOF-5: Zn$_4$O(bdc)$_3$, bdc = benzene-1,4-dicarboxylate/MesMOF-1: Tb$_{16}$(TATB)$_{16}$: TATB = triazine-1,3,5-tribenzoate/SNU-90: [Zn$_4$O(atb)$_2$]$\cdot$22DMF$\cdot$9H$_2$O; atb = aniline-2,4,6-tribenzoate/MIL-101: Cr$_3$F(H$_2$O)$_2$O[(O$_2$C)–C$_6$H$_4$–(CO$_2$)]$_3 \cdot n$H$_2$O/MIL-100(Al): (Al$_3$O(OH)(H$_2$O)$_2$[btc]$_2$)$\cdot$3nH$_2$O; btc = benzene-1,3,5-tricarboxylate/Zr$_6$(μ_3-O)$_4$(μ_3-OH)$_4$(bpdc)$_{5.94}$(L$_1$)$_{0.06}$: L$_1$ = 2,2'-bipyridine-5,5'-dicarboxylate/Zr$_6$-(μ_3-O)$_4$(μ_3-OH)$_4$(L$_2$)$_6 \cdot$64DMF: L$_2$ = 2,2'-bipyridine-5,5'-dibenzoate; ppy = 2-phenyl-pyridine; bpy = 2,2'-bipyridine/CPL-1: [Cu$_2$(pzdc)$_2$(pyz)]$_n$, pzdc = pyrazine-2,3-dicarboxylate, pyz = pyrazine/CPL-2: [Cu$_2$(pzdc)$_2$(bpy)]$_n$, bpy = 4,4'-bipyridine]/MIL-53(Al): [Al(OH)(bdc)]$_n$/Cu-BTC: [Cu$_3$(btc)$_2$]$_n$, btc = benzene-1,3,5-tricarboxylate/[Cd$_2$(L)$\cdot$(H$_2$O)]$\cdot$0.5H$_2$O: L = 4,4'-(hexafluoroisopropylidene)diphthalate/MOF-508: Zn(BDC)(4,4'-Bipy)$_{0.5}\cdot$(DMF)(H$_2$O)$_{0.5}$; BDC = 1,4-benzenedicarboxylic acid; 4,4'-Bipy = 4,4'-bipyridine MIL-68(In): In(OH)(O$_2$C–C$_6$H$_4$–CO$_2$). [c] Ref. = ref. 13 includes the same data.
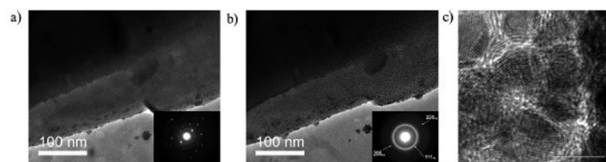
Fig. 13 Before and after TEM images of Ag@MIL-68(In). (a) TEM image of Ag@MIL-68(In) before significant electron beam damage. The inset is an SAED pattern of the MOF. (b) TEM image of Ag@MIL-68(In) after 1 min exposure, showing significant beam damage. The inset is an SAED pattern of the MOF and coalesced Ag. (c) HRTEM image of coalesced Ag particles. Reprinted with permission from ref. 43.


Fig. 15 (a) EPR spectrum of the solid that was isolated after [(NiL$_2$)$_2$(bptc)]$\cdot$2H$_2$O (**2**) was immersed in an EtOH solution of NaAuCl$_4 \cdot$2H$_2$O (3.4 $\times$ 10^{-2} M) for 20 min. Measured at 102 K; $g_\perp$ = 2.177 and $g_\parallel$ = 2.026. (b) XPS for the solid isolated after solid **2** (powder sample) was immersed in the EtOH solution of NaAuCl$_4 \cdot$2H$_2$O (3.4 $\times$ 10^{-2} M) for 5 min. Measured at room temperature. Reprinted with permission from ref. 25.

Fig. 14 PXRD patterns for (a) original host framework [((NiL$_1$)$_3$(bpdc)$_3$]$\cdot$2pyr$\cdot$6H$_2$O (**1**), (b) desolvated host framework **1**, (c) desolvated host solid after immersion in a methanolic solution of AgNO$_3$ for 10 min, (d) after immersion for 18 h, and (e) host-free silver nanoparticles. Reprinted with permission from ref. 24.

salts, type of solvents, and temperature.[14,24–27] The nature of metal seems to dominate the size distribution. Ag has a stronger tendency to aggregate than other noble metals such as Pd, Au, and Pt. The redox active PCPs commonly result in much larger M-NPs than the pore sizes of the PCPs, but the growth of M-NPs is still restricted by PCP matrices. This might be a compromise of the competition between the agglomeration tendency to lower the surface tension of M-NPs and the interaction of functional groups in MOFs with M-NPs, although they are not clearly
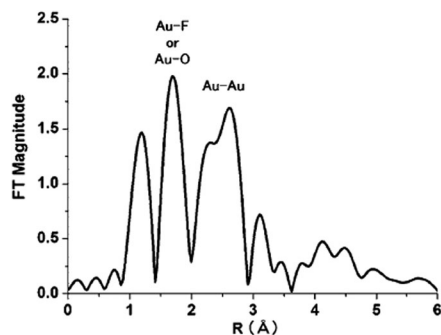
Fig. 16 Au L_{III}-edge FT-EXAFS spectrum for Au@Cd-MOF. The signal at approximately 1.2 Å is due to an experimental artifact. Reprinted with permission from ref. 40.

disclosed. The preparation of M-NPs whose sizes match with the pore sizes of MOFs has been rarely achieved by the functionalization of the MOF surface with strongly interacting groups.[34b] Two MOFs, ZIF-8 and ZIF-90, which have identical topology but different functional groups (methyl vs. aldehyde) at the organic linkers were chosen as the matrices to examine the role of the surface functional groups in the size control of Au NPs. The sizes (average < 2 nm) of Au-NPs formed in ZIF-90 matched with the cavity size of ZIF-90, and very small, including Au_{55}, clusters were homogenously dispersed and stabilized inside the intact crystalline MOF matrix. The aldehyde groups in ZIF-90 act as the surfactant to prevent the growth of M-NPs and stabilize them more effectively compared with the nonfunctionalized and less interacting ZIF-8.

4.2 Localized destruction of frameworks

Robustness of the framework structures is very important for the application of M-NPs@MOFs. On preparation of M-NPs, chemical and thermal stabilities of the MOFs, acidity of metal precursor solutions, and loading amount of M-NPs affect the MOF structure. In the redox active PCP systems, despite the formation of the metal nanoparticles that are much bigger than the aperture size of the networks, the PXRD patterns indicated that the PCP networks were intact, suggesting that the network structures were unaltered by the formation of M-NPs.[24] This was because even if all M-NPs break down the network, only a small percentage of the framework would be destroyed and most of the network would be retained. However, as the immersion time increases, the original host framework can be destroyed as evidenced by PXRD, which might be attributed to the instability of the host in the solutions of metal precursors. The loading of M-NPs leads to a decrease in the surface area of MOFs because the M-NPs not only occupy the cavities of MOFs, but also increase the mass of the system.[34d] In particular, it has been demonstrated that electron beam irradiation during the TEM measurement also destroys the framework structure, which leads to the agglomeration of the particles. As mentioned earlier, in the case of Ag NPs, rapid TEM-induced degradation of MOFs led to agglomeration of the initially formed small Ag_3 clusters and resulted in stable and easily imaged bigger particles.[43]

4.3 Location of M-NPs in/on MOFs

M-NPs can be formed inside the cavities and/or on the external surface of MOFs. Although most of the M-NPs are fabricated inside the cavities of MOFs, some M-NPs can be formed on the surface of the MOFs. To locate the M-NPs, direct evidence should be provided by the TEM tomography technique as mentioned in the previous section. Although TEM is a powerful tool to elucidate the micro- and nano-structure of M-NPs@MOFs, TEM studies involving MOF materials should be performed with great care due to the instability of MOFs upon e-beam exposure.[34b,43] Recently, to avoid any possibilities of aggregation and to immobilize M-NPs inside the pores of MOFs, a double solvent method was employed by using a mixed solution system of hydrophilic and hydrophobic solvents.[37] This method resulted in successful fabrication of Pt NPs inside the pores of MIL-101(Cr) and minimized the deposition of the M-NPs on the outer surface. Zhang et al. prepared Ru NPs immobilized on the surface of a MOF. The material was prepared by dispersion of the MOF in a MeOH solution of $RuCl_3\cdot 3H_2O$ and then introduction of supercritical CO_2, which was followed by heating at 200 °C for 5 h. Ru NPs were stabilized by interaction with the carboxylate groups of the MOF, and aggregation of the particles did not occur.[23] The strong interactions between the M-NPs and the MOF can generate enhanced catalytic activities of the material, compared with unsupported M-NPs.

5. Applications

5.1 Hydrogen storage

To apply MOFs as hydrogen storage materials, various efforts have been made such as pore size tuning,[45] generating accessible metal sites,[4a,46] and fabrication of M-NPs in the MOFs.[14,15,47] In particular, MOFs embedded with Pd NPs have been proven to have enhanced hydrogen uptake capacity at room temperature.[14,15,36,48] The phenomena have been explained by the spillover effect of Pd NPs that split H_2 molecules into hydrogen atoms before they are adsorbed in the MOF, although controversy still exists over the real mechanism. Some other mechanisms such as formation of Pd hydride and hydrogenation of the organic components in the MOFs should be considered as well, and the real mechanism should be proven by appropriate experiments. Besides Pd NPs, Mg NPs were fabricated in a MOF to prepare a hybrid hydrogen storage material.[21] The material Mg-NPs@MOF adsorbs hydrogen both by physi- and chemi-sorption, exhibiting a synergistic effect between them. It increases the isosteric heat of H_2 physisorption compared to pristine MOF and decreases the chemisorption/desorption temperatures by 200 °C compared to bare Mg powder. At 200 °C and 30 bar, 99% of Mg was converted to MgH_2, from which H_2 molecules could be released at $T > 250$ °C.[21]
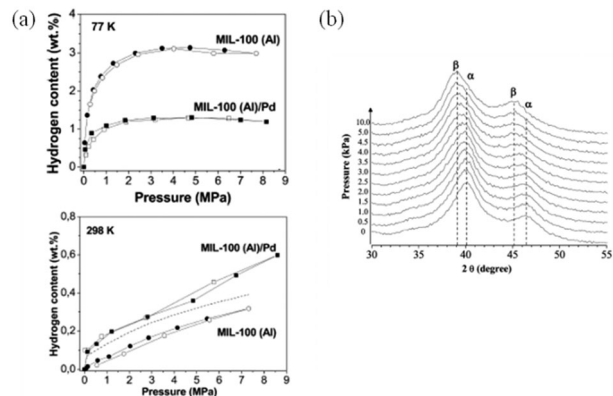
Suh et al. reported that when Pd NPs (< 5 nm) were fabricated in a MOF solid (**5**) by the redox reaction between Pd(II) ions and **5** incorporating redox active organic species (ntb^{3-}), the H_2 uptake capacity depended on the amount of Pd NPs loaded in the MOF.[14] The MOF loaded with 3 wt% Pd NPs showed significantly decreased N_2 and CO_2 uptake capacities because of the introduced counter anions (NO_3^-) and Pd NPs
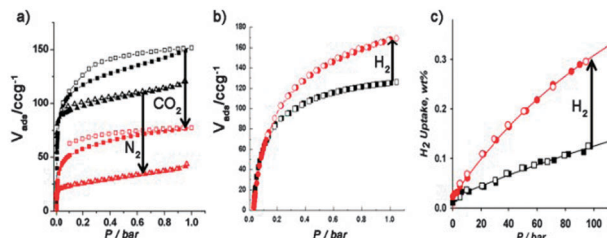
Fig. 17 Gas adsorption (solid symbols) and desorption (open symbols) isotherms for 3 wt% Pd NPs@$5^{0.54+}(NO_3)_{0.54}$ (red) and for the apohost **5** (black). (a) N_2 adsorption at 77 K and CO_2 adsorption at 195 K. (b) H_2 (circles) at 77 K. (c) Excess amount of H_2 uptake at 298 K up to 95 bar. Reprinted with permission from ref. 14.


Fig. 18 (a) Comparison of H_2 adsorption (solid symbols) and desorption (open symbols) isotherms at 77 K and 298 K of MIL-100(Al) and Pd@MIL-100(Al). The dashed line is calculated from the addition of the quantity of H_2 required for the formation of the bulk β-Pd hydride and the amount of physisorbed H_2 by Pd-free MIL-100(Al). (b) *In situ* PXRD measured during the hydrogen adsorption in Pd NPs at room temperature and pressure up to 10 kPa, indicating formation of β-Pd hydride. Reprinted with permission from ref. 15.

that occupied the pore space of the oxidized MOF (Fig. 17a). Contrary to N_2 and CO_2 adsorptions, Pd-NPs (3 wt%)@SNU-3 (**5**) showed enhanced H_2 uptake capacities at 77 K and 1 atm as well as at room temperature. The H_2 uptake capacity at 77 K and 1 atm was increased to 1.48 wt% from 1.03 wt% for the pristine MOF (Fig. 17b). The H_2 uptake capacity at room temperature and 95 bar was increased to 0.30 wt% for the Pd NPs loaded sample, compared with 0.13 wt% for the pristine MOF (Fig. 17c). Considering the decreased surface area and the increase in the mass for the Pd loaded sample, the effective enhancement factor of H_2 uptake by Pd NPs was 350% at 77 K.[14] The effect of incorporated Pd NPs on increasing the H_2 uptake capacity was 230% at room temperature and 95 bar. Although the Pd NPs loaded in the MOF did not provide greater isosteric heat of H_2 adsorption than the pristine MOF, the increased hydrogen uptakes were explained by the spillover effect of Pd NPs, which dissociate H_2 molecules into H atoms before adsorption on the surface of the MOF.

Latroche and Ferey *et al.* also reported that the composite material Pd@MIL-100(Al), which was prepared by impregnation of a Pd precursor followed by treatment with hydrogen stream, showed increased hydrogen uptake at room temperature.[15] After loading 10 wt% Pd in MIL-100(Al), the hydrogen sorption capability at 77 K decreased as compared with that of MIL-100(Al), whereas maximum hydrogen capacity at 298 K increased as shown in Fig. 18a. The careful comparison of the hydrogen isotherms measured for MIL-100(Al) and MIL-100(Al)/Pd at 298 K reveals the different sorption properties. The isotherm of MIL-100(Al) at room temperature shows a linear trend, as generally reported for microporous material, but the isotherm of the Pd@MIL-100(Al) composite displays a steep increase below 0.1 MPa followed by a constant increase with pressure and an almost similar slope to that for the MIL-100(Al) isotherm. The different isotherm for Pd@MIL-100(Al) originates from the formation of Pd hydride during the H_2 adsorption at room temperature. *In situ* PXRD patterns measured during hydrogen uptake evidenced this, showing that increase in pressure from 0.5 to 4.5 kPa led to the formation of β-Pd hydride (Fig. 18b). When the sum of the quantity of H_2 required for formation of the bulk β-Pd hydride and the amount of physisorbed H_2 by Pd-free MIL-100(Al) was calculated (dashed lines in Fig. 18b), the actual uptake amount of the Pd@MIL-100(Al)

composite exceeded it. It was explained that the spillover effect of Pd NPs took place, which promoted the dissociation of H_2 molecules into H atoms, to result in the enhanced hydrogen uptake capacity.

As an alternative to MOFs, a covalent organic framework (COF) was used as the support for fabricating Pd NPs.[48] Fischer's group prepared the Pd@COF-102 nanocomposite by the gas-phase infiltration of $[Pd(\eta^3-C_3H_5)(\eta^3-C_5H_5)]$ into COF-102 and subsequent photodecomposition. The resulting material Pd@COF-102 exhibited enhanced hydrogen uptake by a factor of 2–3 at room temperature and 20 bar, compared to pristine COF (Fig. 19). The enhancement was attributed to Pd-hydride formation as well as hydrogenation of organic residues originating from the metal precursor, as evidenced by MAS ^{13}C NMR.

Recently, Suh's group reported Mg-NCs@SNU-90′ as a hybrid hydrogen storage material. It adsorbed hydrogen by physisorption at low temperatures and by chemisorption at high temperatures, particularly showing the synergistic effect on both.[21]
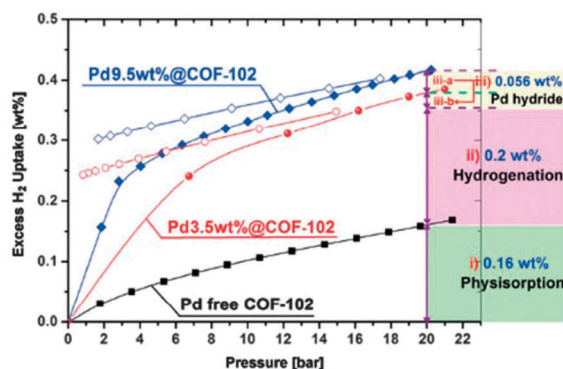
Fig. 19 Hydrogen sorption isotherms of pristine COF-102 (black), Pd(3.5 wt%)@COF-102 (red), and Pd(9.5 wt%)@COF-102 (blue) at 298 K. Reprinted with permission from ref. 48.
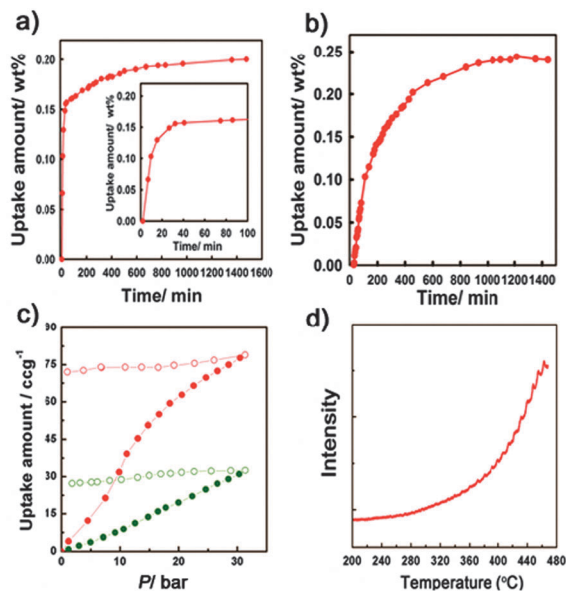
Fig. 20 Chemical adsorption of H_2 in Mg(10.5 wt%)@SNU-90′. (a) The H_2 absorption kinetics at 325 K and 80 bar. Inset: data with a magnified time scale. (b) The H_2 absorption kinetics at 415 K and 40 bar. (c) The H_2 adsorption isotherms at 473 K in Mg(6.52 wt%)@SNU-90′ (green, ●) and Mg(10.5 wt%)@SNU-90′ (red, ●). (d) Temperature programmed desorption mass spectroscopy (TPD-MS) data; $m/z = 2$, measured under argon. Reprinted with permission from ref. 21.

The hydrogen physisorption data for various samples of Mg@SNU-90′ showed that the BET surface area, pore volume, and H_2 uptake capacities at 77 K and 1 atm decreased as the amount of Mg embedded in MOF increased, because Mg NCs occupied the pore space of the MOF. However, the zero-coverage isosteric heat of H_2 physisorption increased as the amount of embedded Mg increased up to 11.6 kJ mol^{-1} for Mg(10.5 wt%)@SNU-90′ compared with 4.55 kJ mol^{-1} for SNU-90′. The hydrogen physisorption capacity in the MOF at 298 K and 80 bar also improved by *ca.* 20% due to the embedded Mg NCs. Contrary to the physisorption, the H_2 chemisorption capacities of the material increased as the temperature and the amount of loaded Mg increased. The hydrogen uptake capacity in Mg(10.5 wt%)@SNU-90′ at 473 K and 30 bar reaches 0.71 wt% (Fig. 20), which corresponded to 7.5 wt% H_2 adsorption in Mg alone, implying that 99% of Mg was converted to MgH$_2$ upon H_2 absorption. Desorption of H_2 occurred at 573 K and 1 atm, as evidenced by temperature programmed desorption mass spectroscopy. The Mg NCs embedded in the MOF lowered the H_2 chemisorption/ desorption temperatures by >200 K than those of bare Mg(50–100 μm). After the H_2 chemisorption at 473 K and 30 bar, the HRTEM images of Mg@SNU-90′ indicated that the crystal morphology of Mg was maintained but the crystal size was remarkably increased. The excessive expansion during the H_2 chemisorption processes at high temperature and pressure can be explained by the three dimensional Ostwald ripening.

5.2 Heterogeneous catalysis

Some MOFs containing NPs have shown excellent activities in many organic reactions due to the confinement effect as well as

the limitation of the particles that remain constrained avoiding growth after catalytic reactions. Recently, catalysis by M-NPs@MOF has been well reviewed,[49] and here we will briefly introduce various reactions catalyzed by M-NPs@MOF, classifying them by reaction types.

5.2.A LIQUID PHASE CATALYTIC REACTIONS: AEROBIC OXIDATION OF ALCOHOLS AND OLEFIN HYDROGENATION. Various supported metal nanoparticles have been utilized in a wide range of applications, especially catalysis.[50] Metal nanoparticle incorporated MOFs are one of the most promising heterogeneous catalysts. Among liquid phase catalytic reactions over M-NPs@MOF, the oxidation reaction of alcohol is the most well known reaction. Haruta *et al.* compared the catalytic activities and the product selectivities of Au NPs loaded in various MOFs in aerobic oxidation of alcohol.[17] Generally, the oxidation of benzyl alcohol yields a mixture of benzaldehyde and benzoic acid, and a base should be usually added to accelerate the reaction by deprotonating the alcohol. While Au/polymer gel showed low selectivity to produce 36% benzoic acid and 49% benzaldehyde, respectively, Au@MOF-5 and Au@MIL-53(Al) exhibited selective catalytic activity to produce methyl benzoate, and Au@Cu-PCPs showed high selectivity toward benzaldehyde. These phenomena were explained by the different degrees of surface acidity of each MOFs or PCPs, which tuned unique product selectivity. In addition, Au NPs in PCPs exhibited high catalytic activity in liquid phase benzyl alcohol oxidation even in the absence of base. The proposed mechanism for benzyl alcohol oxidation over Au@PCP is compared with that over Au/AC (AC: activated carbon) in Fig. 21.

Similarly, Au@MIL-101, which was prepared by deposition of Au-PVP colloids onto MIL-101, exhibited high catalytic activities in liquid-phase aerobic oxidation of various alcohols.[19] The catalyst Au@MIL-101 is very efficient because it can catalyze the aerobic
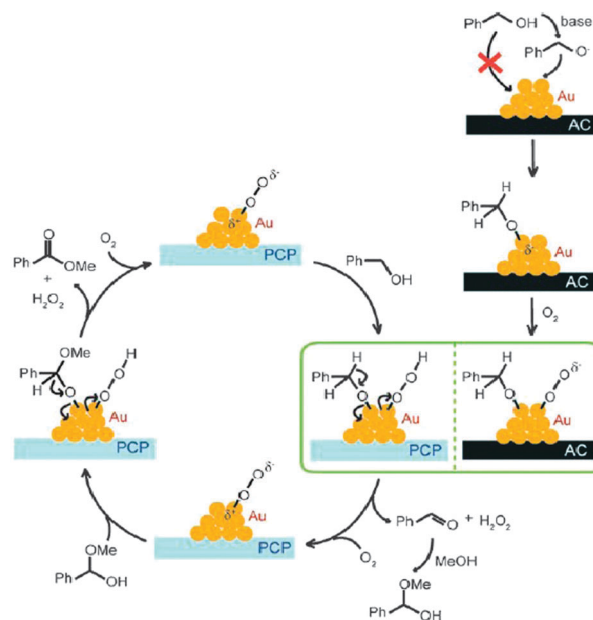
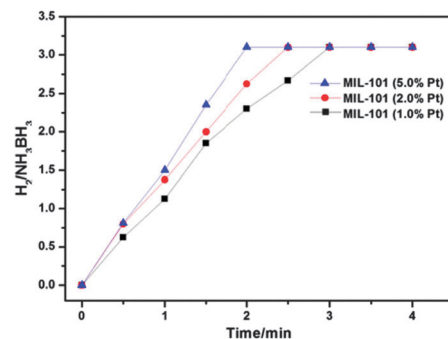**Fig. 21** Plausible pathways for benzyl alcohol oxidation over Au/PCPs and Au/AC. Reprinted with permission from ref. 17.

This journal is © The Royal Society of Chemistry 2013

Chem. Soc. Rev., 2013, **42**, 1807–1824 | **1821**

oxidation reaction in the absence of water or base. It was suggested that the highly dispersed Au NPs and the electron donating effect of aryl rings of substituted benzyl alcohols to the Au NPs within the large cages of the MIL-101 provided the high activity of the catalyst under the reaction conditions.

The other representative catalytic reaction over metal@PCPs is olefin hydrogenation. Pd NPs loaded in MOF-5 showed a high catalytic activity in styrene hydrogenation, which is comparable to that of Pd NPs on AC.[36] While large molecules such as 1-octene and *cis*-cyclooctene could not effectively access the pores resulting in low conversion, hydrogenation of styrene over Pd@MOF-5 produced ethylbenzene with high catalytic activity. By changing the reduction conditions, catalytic performance could be altered, and the treatment with H_2 stream at higher temperature afforded a positive effect on this reaction.

5.2.b LIQUID PHASE CATALYTIC REACTIONS: C–C COUPLING REACTIONS. C–C coupling reactions such as Suzuki–Miyaura, Ullmann, Heck, and Sonogashira coupling reactions are some of the most important and useful reactions in organic synthesis. Palladium-catalyzed C–C bond formations have been intensively studied, and Pd NPs incorporating MOFs were examined as C–C coupling catalysts. MIL series and surface modified MOFs were mainly used as supports due to their high stability in aqueous solution as well as in organic solvent (Fig. 22). The Pd@ED-grafted-MIL-101(Cr) and Pd@APS-grafted-MIL-101(Cr) (ED = ethylenediamine, APS = 3-aminopropyltrialkoxysilane), which were obtained by anion exchange reactions followed by NaBH₄ reduction in amine-functionalized MIL-101(Cr), had high activities in the Heck reaction of acrylic acid with iodobenzene. Their activities were comparable with that of a commercial Pd/C catalyst (1.09 wt% Pd) after a certain induction period (0.5–1 h).[51] Pd@MIL-101(Cr) showed good recyclability. It was also reported that Pd@MIL-101(Cr) catalyzed the one-pot cascade synthesis of methyl isobutyl ketone (MIBK) from acetone.[52] Pd@MIL-101(Cr) was also tested for Suzuki–Miyaura and Ullmann coupling reactions.[53] It catalyzed the coupling reaction between 4-chloroanisole and phenylboronic acid in the presence of various bases. This provided an important example since C–Cl bond activation requires much harsher reaction conditions than for

Fig. 22 Schematic descriptions of Heck, Suzuki–Miyaura, Ullmann coupling reactions. Reprinted with permission from ref. 51 and 53.

Fig. 23 Hydrogen generation from aqueous NH₃BH₃ in the presence of Pt@MIL-101 catalyst at room temperature. Pt : AB (molar ratio) = 0.0014, 0.0029, and 0.0071 at Pt loadings of 1.0, 2.0 and 5.0%, respectively. Reprinted with permission from ref. 37.
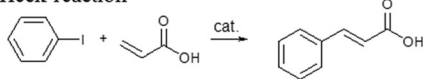
the C–Br and C–I bonds. The catalytic activities of Pd@MIL-101(Cr) for Ullmann homocoupling reactions of various aryl chlorides were also examined in air as well as under a nitrogen atmosphere. The results revealed high reaction yield (>96%) under both reaction conditions. After the reaction, the Pd@MIL-101(Cr) catalyst was easily recovered and reused five times without any loss of efficiency.

5.2.c LIQUID PHASE AMMONIA BORANE HYDROLYSIS. Ammonia borane is one of the promising hydrogen storage materials, from which H_2 can be released by either hydrolysis or pyrolysis. Xu *et al.* recently reported that Pt-NPs@MIL-101 (size of Pt NPs, average 1.8 ± 0.2 nm) catalyzed liquid phase ammonia borane (NH₃BH₃, AB) hydrolysis.[37] When the aqueous AB was introduced into the reaction flask containing Pt@MIL-101 with vigorous stirring, H_2 was produced from aqueous AB at room temperature (Fig. 23). The rate of hydrolysis of AB is 1.0×10^4 L_{H2} mol_{Pt}^{-1} min^{-1}, 2 times faster than that of 2 wt% Pt/γ-Al₂O₃, the most active Pt catalyst reported so far for this reaction. It was found that the productivity of H_2 over the Pt@MIL-101 catalyst remains unchanged after five runs, indicating the high durability of the catalyst. Since the byproduct (BO^{2-}) formed from AB hydrolysis is soluble in water, the spent fuel can be removed by washing with water and the catalyst can be reused.
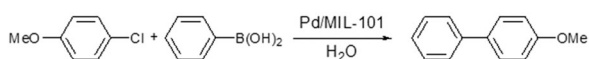
5.2.d GAS PHASE CATALYTIC REACTION: CO OXIDATION. The liquid-phase catalytic reactions over pristine MOFs or M-NPs@MOFs have been actively exploited. However, their catalytic properties for gaseous reactions have been rarely reported. El-Shall *et al.* reported catalytic oxidation of CO to CO_2 by the bimetallic nanocatalyst systems incorporated into MIL-101.[19] The Pd NPs@MIL-101 catalyst containing 2.9 wt% Pd NPs showed the highest catalytic activity among catalysts with various amounts of Pd NPs, and small sized Pd nanocrystals mainly participated in the catalytic reaction. While Cu NPs@MIL-101 showed full conversion at high temperature (289 °C), the mixed Pd–Cu catalyst exhibited full conversion at 152 °C, revealing significantly enhanced catalytic function compared with the Cu NPs-only catalyst, which is possibly due to the formation of a PdCu nanoalloy (Fig. 24).

Xu *et al.* also reported the catalytic CO oxidation by Au NPs embedded in ZIF-8,[39] as well as by Pt NPs embedded in MIL-101.[37]
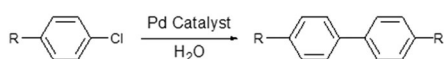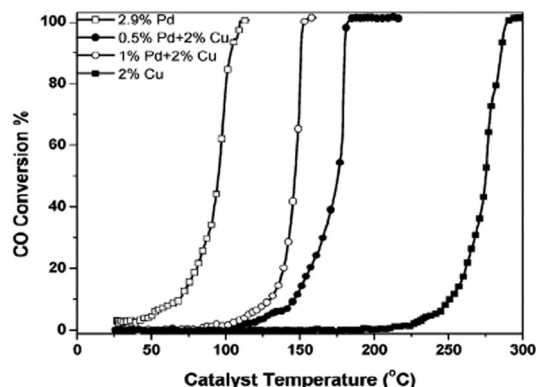
1822 | *Chem. Soc. Rev.*, 2013, **42**, 1807–1824

This journal is © The Royal Society of Chemistry 2013

Fig. 24 CO oxidation to CO_2 on Pd, Cu, and mixed Pd–Cu nanocatalysts supported in MIL-101. Reprinted with permission from ref. 20.
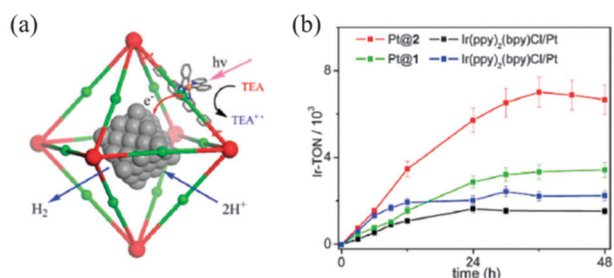
Fig. 25 (a) A scheme showing the synergistic photocatalytic hydrogen evolution process *via* photoinjection of electrons from the light-harvesting MOF framework into the Pt NPs. (b) Time-dependent hydrogen evolution curves. **1** and **2** in (b) indicate $Zr_6(\mu_3\text{-O})_4(\mu_3\text{-OH})_4(bpdc)_{5.94}(L_1)_{0.06}$ and $Zr_6(\mu_3\text{-O})_4(\mu_3\text{-OH})_4(L_2)_6 \cdot 64DMF$, respectively. Reprinted with permission from ref. 18.

For Au@ZIF-8, the CO oxidation activities improved with increasing amount of Au loaded in ZIF-8, as evidenced by the decrease of the temperature for 50% conversion of CO. For Pt@MIL-101, while MIL-101 exhibited no catalytic activity for CO oxidation in the temperature range 25–180 °C, the 5% Pt@MIL-101 started to show activity at 50 °C. The CO to CO_2 conversion increased suddenly at 100 °C and complete conversion occurred at 150 °C. Arrhenius plots showed that the activation energy was 40.7 kJ mol^{-1}. Pt@MIL-101 showed stable activity, keeping 100% CO conversion for 150 min at 175 °C. After catalytic reaction, the crystallinity of the Pt@MIL-101 host matrix remained unchanged with no large Pt particle aggregation.

5.2.E PHOTOCATALYTIC HYDROGEN EVOLUTION. The Pt NPs loaded in photoactive MOFs, $Zr_6(\mu_3\text{-O})_4(\mu_3\text{-OH})_4(bpdc)_{5.94}(L_1)_{0.06}$ and $Zr_6(\mu_3\text{-O})_4(\mu_3\text{-OH})_4(L_2)_6$, were found to be efficient photocatalysts for hydrogen evolution from water, giving higher turnover frequencies and higher turnover numbers than those of the homogeneous analogs (Fig. 25).[18] The radicals, $[Ir^{III}(ppy)_2(bpy^{\bullet-})]$, generated in the MOFs by TEA-mediated photoreduction can transfer electrons to the entrapped Pt NPs to reduce protons of water. The highest hydrogen evolution turnover number (TON) based on Ir phosphors (Ir-TON) in 6 h was 1620, showing high photochemical quantum yield.

6. Concluding comments

In last few decades, dramatic advancement has been made in metal–organic frameworks. In particular, various synthetic strategies for incorporating M-NPs in porous MOFs have been developed, and the applications of those materials have been successfully demonstrated. By the choice of well-designed metal or organic molecular building blocks, redox-active PCPs could be synthesized, and the simple immersion of the redox-active PCPs in the metal precursor solutions produced M-NPs embedded in the PCPs at room temperature, in the absence of extra reducing agents and capping agents. In addition, to initially deposit metal precursors in the porous MOFs, other methods such as CVD, impregnation of metal solution, and solid-grinding have been also employed. When the reduction steps such as thermal hydrogenolysis were followed, various M-NPs@MOFs were yielded. Recently, fabrication of M-NPs in a MOF has been made by the irradiation of UV light on the metal ion impregnated MOF or by visible light irradiation on the metal ion included photoactive MOF. In addition, presynthesized M-NPs stabilized by a polymer are included in a MOF by synthesizing MOFs in the presence of the M-NPs capped by a polymer. The advantages of using MOFs as supports for M-NPs are the following: (1) the confinement effect of MOFs provides limited growth of M-NPs and generates rather uniform and small sized M-NPs, (2) the structural diversity of MOFs having different pore sizes and channel systems offers the choice of appropriate MOFs for M-NPs generation, (3) the organic parts of a MOF can interact with M-NPs and stabilize them without an extra stabilizing agent. Even though M-NPs bigger than the pore sizes are generally formed, the MOF frameworks are maintained in most of the cases. For this phenomenon, it has been argued that MOF frameworks are apt to be degraded upon TEM electron irradiation, which induces the agglomerization of the small metal clusters into bigger M-NPs. To characterize nanocomposites of M-NPs@MOFs, various techniques have been used such as ICP, IR, NMR, EPR spectroscopy, elemental analysis, EXAFS, XPS, TEM, electron tomography, and PXRD, which are described in this review. Using the resultant M-NPs@MOFs, enhanced hydrogen storage, liquid- and gas-phase catalytic reactions, and photocatalytic hydrogen evolution have been successfully demonstrated. In the coming years, more facile and inexpensive preparative methods for M-NPs@MOFs should be developed, and the multifaceted efforts would be accompanied to show the useful applications of these nanocomposites. Furthermore, the nanomaterials impregnated in MOFs should be extended from metals to a wide range of chalcogenides and pnictide semiconductors, and some transition-metal oxides.[54] Those nanocomposites would exhibit diverse functionalities, and they might provide environmentally benign and commercially useful catalyst systems. The fabrication of the various compounds in MOFs will be a highly promising field for the future.

Acknowledgements

This journal is © The Royal Society of Chemistry 2013

Chem. Soc. Rev., 2013, **42**, 1807–1824 | **1823**

Notes and references

1 S. T. Batten, N. R. Champness, X.-M. Chen, J. Garcia-Martinez, S. Kitagawa, L. Ohrstrom, M. O'Keeffe, M. P. Suh and J. Reedijk, *CrystEngComm*, 2012, **14**, 3001–3004.

2 O. M. Yaghi, M. O'Keeffe, N. W. Ockwig, H. K. Chae, M. Eddaoudi and J. Kim, *Nature*, 2003, **423**, 705–714.

3 (a) K. L. Mulfort, O. K. Farha, C. L. Stern, A. A. Sarjeant and J. T. Hupp, *J. Am. Chem. Soc.*, 2009, **131**, 3866–3868; (b) J. Yang, A. Grzech, F. M. Mulder and T. J. Dingemans, *Chem. Commun.*, 2011, **47**, 5244–5246.

4 (a) Y.-G. Lee, H. R. Moon, Y. E. Cheon and M. P. Suh, *Angew. Chem., Int. Ed.*, 2008, **47**, 7741–7745; (b) Y. E. Cheon, J. Park and M. P. Suh, *Chem. Commun.*, 2009, 5436–5438; (c) H. J. Park and M. P. Suh, *Chem. Commun.*, 2010, **46**, 610–612; (d) H. R. Moon, N. Kobayashi and M. P. Suh, *Inorg. Chem.*, 2006, **45**, 8672–8676; (e) T. K. Kim and M. P. Suh, *Chem. Commun.*, 2011, **47**, 4258–4560; (f) H. J. Park, Y. E. Cheon and M. P. Suh, *Chem.–Eur. J.*, 2010, **16**, 11662–11669.

5 A. Corma, H. Garcia and F. X. L. i Xamena, *Chem. Rev.*, 2010, **110**, 4606–4655.

6 (a) A. Lan, K. Li, H. Wu, D. H. Olson, T. J. Emge, W. Ki, M. Hong and J. Li, *Angew. Chem., Int. Ed.*, 2009, **48**, 2334–2338; (b) J. Liu, F. Sun, F. Zhang, Z. Wang, R. Zhang, C. Wang and S. Qiu, *J. Mater. Chem.*, 2011, **21**, 3775–3778.

7 (a) I. T. Weber, A. J. G. de Melo, M. A. de M. Lucena, M. O. Rodrigues and S. A. Junior, *Anal. Chem.*, 2011, **83**, 4720–4723; (b) P. Horcajada, C. Serre, D. Grosso, C. Boissiere, S. Perruchas, C. Sanchez and G. Ferey, *Adv. Mater.*, 2009, **21**, 1931–1935.

8 J.-T. Lue, *J. Phys. Chem. Solids*, 2001, **62**, 1599–1612.

9 (a) K. L. Kelly, E. Coronado, L. L. Zhao and G. C. Schatz, *J. Phys. Chem. B*, 2003, **107**, 668–677; (b) A. R. Tao, S. Habas and P. Yang, *Small*, 2008, **4**, 310–325.

10 C. Burda, X. Chen, R. Narayanan and M. A. El-Sayed, *Chem. Rev.*, 2005, **105**, 1025–1102.

11 (a) K. Aslan, M. Wu, J. R. Lakowicz and C. D. Geddes, *J. Am. Chem. Soc.*, 2007, **129**, 1524–1525; (b) S. H. Joo, J. Y. Park, C.-K. Tsung, Y. Yamada, P. Yang and G. A. Somorjai, *Nat. Mater.*, 2009, **8**, 126–131.

12 (a) S. H. Joo, S. J. Choi, I. Oh, J. Kwak, Z. Liu, O. Terasaki and R. Ryoo, *Nature*, 2001, **412**, 169–172; (b) H. Song, R. M. Rioux, J. D. Hoefelmeyer, R. Komor, K. Niesz, M. Grass, P. Yang and G. A. Somorjai, *J. Am. Chem. Soc.*, 2006, **128**, 3027–3037.

13 M. Meilikhov, K. Yusenko, D. Esken, S. Turner, G. V. Tendeloo and R. A. Fischer, *Eur. J. Inorg. Chem.*, 2010, 3701–3714.

14 Y. E. Cheon and M. P. Suh, *Angew. Chem., Int. Ed.*, 2009, **48**, 2899–2903.

15 C. Zlotea, R. Campesi, F. Cuevas, E. Leroy, P. Dibandjo, C. Volkringer, T. Loiseau, G. Ferey and M. Latroche, *J. Am. Chem. Soc.*, 2010, **132**, 2991–2997.

16 D. Esken, X. Zhang, O. I. Lebedev, F. Schröder and R. A. Fischer, *J. Mater. Chem.*, 2009, **19**, 1314–1319.

17 T. Ishida, M. Nagaoka, T. Akita and M. Haruta, *Chem.–Eur. J.*, 2008, **14**, 8456–8460.

18 C. Wang, K. E. deKrafft and W. Lin, *J. Am. Chem. Soc.*, 2012, **134**, 7211.

19 H. Liu, Y. Liu, Y. Li, Z. Tang and H. Jiang, *J. Phys. Chem. C*, 2010, **114**, 13362–13369.

20 M. S. El-Shall, V. Abdelsayed, A. E. R. S. Khder, H. M. A. Hassan, H. M. El-Kaderi and T. E. Reich, *J. Mater. Chem.*, 2009, **19**, 7625–7631.

21 D.-W. Lim, J. W. Yoon, K. Y. Ryu and M. P. Suh, *Angew. Chem., Int. Ed.*, 2012, **51**, 9814–9817.

22 F. Schröder and R. A. Fischer, *Top. Curr. Chem.*, 2010, **293**, 77–113.

23 Y. Zhao, J. Zhang, J. Song, J. Li, J. Liu, T. Wu, P. Zhang and B. Han, *Green Chem.*, 2011, **13**, 2078–2082.

24 H. R. Moon, J. H. Kim and M. P. Suh, *Angew. Chem., Int. Ed.*, 2005, **44**, 1261–1265.

25 M. P. Suh, H. R. Moon, E. Y. Lee and S. Y. Jang, *J. Am. Chem. Soc.*, 2006, **128**, 4710–4718.

26 Y. E. Cheon and M. P. Suh, *Chem.–Eur. J.*, 2008, **14**, 3961–3967.

27 H. R. Moon and M. P. Suh, *Eur. J. Inorg. Chem.*, 2010, 3795–3803.

28 M. P. Suh, *Adv. Inorg. Chem.*, 1997, **44**, 93–146.

29 M. P. Suh, Y. E. Cheon and E. Y. Lee, *Chem.–Eur. J.*, 2007, **13**, 4208–4215.

30 Y. Wei, S. Han, D. A. Walker, P. E. Fuller and B. A. Grzybowski, *Angew. Chem., Int. Ed.*, 2012, **51**, 7435–7439.

31 M. J. Hampden-Smith and T. T. Kodas, *Chem. Vap. Deposition*, 1995, **1**, 8–23.

32 C. L. Bowes, A. Malek and G. A. Ozin, *Chem. Vap. Deposition*, 1996, **2**, 97–103.

33 S. Hermes, M.-K. Schröter, R. Schmid, L. Khodeir, M. Muhler, A. Tissler, R. W. Fischer and R. A. Fischer, *Angew. Chem., Int. Ed.*, 2005, **44**, 6237–6241.

34 (a) F. Schröder, D. Esken, M. Cokoja, M. W. E. van den Berg, O. I. Lebedev, G. V. Tendeloo, B. Walaszek, G. Buntkowsky, H.-H. Limbach, B. Chaudret and R. A. Fischer, *J. Am. Chem. Soc.*, 2008, **130**, 6119–6130; (b) D. Esken, S. Turner, O. I. Lebedev, G. V. Tendeloo and R. A. Fischer, *Chem. Mater.*, 2010, **22**, 6393–6401; (c) Y. K. Park, S. B. Choi, H. J. Nam, D.-Y. Jung, H. C. Ahn, K. Choi, H. Furukawa and J. Kim, *Chem. Commun.*, 2010, **46**, 3086–3088; (d) J. Hermannsdörfer and R. Kempe, *Chem.–Eur. J.*, 2011, **17**, 8071–8077.

35 F. Schröder, S. Henke, X. Zhang and R. A. Fischer, *Eur. J. Inorg. Chem.*, 2009, 3131–3140.

36 M. Sabo, A. Henschel, H. Fröde, E. Klemm and S. Kaskel, *J. Mater. Chem.*, 2007, **17**, 3827–3832.

37 A. Aijaz, A. Karkamkar, Y. J. Choi, N. Tsumori, E. Rönnebro, T. Autrey, H. Shioyama and Q. Xu, *J. Am. Chem. Soc.*, 2012, **134**, 13926–13929.

38 R. Ameloot, M. B. J. Roeffaers, G. D. Cremer, F. Vermoortele, J. Hofkens, B. F. Sels and D. E. De Vos, *Adv. Mater.*, 2011, **23**, 1788–1791.

39 H.-L. Jiang, B. Liu, T. Akita, M. Haruta, H. Sakurai and Q. Xu, *J. Am. Chem. Soc.*, 2009, **131**, 11302–11303.

40 H.-L. Jiang, Q.-P. Lin, T. Akita, B. Liu, H. Ohashi, H. Oji, T. Honma, T. Takei, M. Haruta and Q. Xu, *Chem.–Eur. J.*, 2011, **17**, 78–81.

41 (a) M. Okumura, S. Tsubota and M. Haruta, *J. Mol. Catal. A: Chem.*, 2003, **199**, 73–84; (b) M. Okumura, K. Tanaka, A. Ueda and M. Haruta, *Solid State Ionics*, 1997, **95**, 143–149.

42 G. Lu, S. Li, Z. Guo, O. K. Farha, B. G. Hauser, X. Qi, Y. Wang, X. Wang, S. Han, X. Liu, J. S. DuChene, H. Zhang, Q. Zhang, X. Chen, J. Ma, S. C. J. Loo, W. D. Wei, Y. Yang and J. T. Hupp, *Nat. Chem.*, 2012, **4**, 310–316.

43 R. J. T. Houk, B. W. Jacobs, F. E. Gabaly, N. N. Chang, A. A. Talin, D. D. Graham, S. D. House, I. M. Robertson and M. D. Allendorf, *Nano Lett.*, 2009, **9**, 3413–3418.

44 S. Turner, O. I. Lebedev, F. Schroder, D. Esken, R. A. Fischer and G. V. Tendeloo, *Chem. Mater.*, 2008, **20**, 5622–5627.

45 (a) S. Ma, D. Sun, M. Ambrogio, J. A. Fillinger, S. Parkin and H.-C. Zhou, *J. Am. Chem. Soc.*, 2007, **129**, 1858–1859; (b) J. L. Belof, A. C. Stern, M. Eddaoudi and B. Space, *J. Am. Chem. Soc.*, 2007, **129**, 15202–15210.

46 (a) M. Dinca and J. R. Long, *J. Am. Chem. Soc.*, 2007, **129**, 11172–11176; (b) S. S. Kaye and J. R. Long, *J. Am. Chem. Soc.*, 2005, **127**, 6506–6507; (c) K. L. Mulfor and J. T. Hupp, *J. Am. Chem. Soc.*, 2007, **129**, 9604–9605.

47 (a) Y. Li and R. T. Yang, *J. Am. Chem. Soc.*, 2006, **128**, 726–727; (b) Y. Li and R. T. Yang, *J. Am. Chem. Soc.*, 2006, **128**, 8136–8137.

48 S. B. Kalidindi, H. Oh, M. Hirscher, D. Esken, C. Wiktor, S. Turner, G. V. Tendeloo and R. A. Fischer, *Chem.–Eur. J.*, 2012, **18**, 10848–10856.

49 A. Dhakshinamoorthy and H. Garcia, *Chem. Soc. Rev.*, 2012, **41**, 5262–5284.

50 R. M. Crooks, M. Zhao, L. Sun, V. Chechik and L. K. Yeung, *Acc. Chem. Res.*, 2001, **34**, 181–190.

51 Y. K. Hwang, D.-Y. Hong, J.-S. Chang, S. H. Jhung, Y.-K. Seo, J. Kim, A. Vimont, M. Daturi, C. Serre and G. Férey, *Angew. Chem., Int. Ed.*, 2008, **47**, 4144–4148.

52 Y. Pan, B. Yuan, Y. Li and D. He, *Chem. Commun.*, 2010, **46**, 2280–2282.

53 B. Yuan, Y. Pan, Y. Li, B. Yin and H. Jiang, *Angew. Chem., Int. Ed.*, 2010, **49**, 4054–4058.

54 (a) M. Müller, S. Hermes, K. Kähler, M. W. E. van den Berg, M. Muhler and R. A. Fischer, *Chem. Mater.*, 2008, **20**, 4576–4587; (b) M. Müller, X. Zhang, Y. Wang and R. A. Fischer, *Chem. Commun.*, 2009, 119–121.

1824 | *Chem. Soc. Rev.*, 2013, **42**, 1807–1824

This journal is © The Royal Society of Chemistry 2013